

**MICROMECHANICS, FRACTURE MECHANICS AND
GAS PERMEABILITY OF COMPOSITE LAMINATES
FOR CRYOGENIC STORAGE SYSTEMS**

By

**Sukjoo Choi, Graduate Student
Bhavani V. Sankar, Newton C. Ebaugh Professor
Department of Mechanical & Aerospace Engineering
University Of Florida, Gainesville, FL 32611-6250**

2005

TABLE OF CONTENTS

| | <u>page</u> |
|---|-------------|
| LIST OF TABLES | iii |
| LIST OF figures | iv |
| ABSTRACT | vi |
| INTRODUCTION | 1 |
| Micromechanics Analysis of Laminated Composites at Cryogenic Conditions | 3 |
| Fracture Toughness of a Transverse Crack at Cryogenic Conditions | 4 |
| Permeability of Graphite Fiber Composite Materials at Cryogenic Conditions..... | 6 |
| MICROMECHANICS METHODS TO PREDICT MICRO-STRESSES IN | |
| LAMINATED COMPOSITES AT CRYOGENIC TEMPERATURES | 8 |
| Micromechanics Model | 8 |
| Thermo-Elastic Properties of the Composite Constituents..... | 10 |
| Estimation of Thermo-Elastic Constants | 12 |
| Effects of Fiber Volume Fraction | 16 |
| Prediction of Stresses at Microscopic Level..... | 17 |
| Application to the Liquid Hydrogen Composite Tank | 20 |
| FRACTURE TOUGHNESS FOR A TRANSVERSE CRACK IN LAMINATED | |
| COMPOSITES AT CRYOGENIC TEMPERATURES | 25 |
| Stress Singularities at a Crack-tip Normal to a Ply-interface | 25 |
| Fracture Toughness at Room Temperature..... | 28 |
| Fracture Toughness at Cryogenic Temperatures | 32 |
| PERMEABILITY TESTING OF COMPOSITE MATERIALS FOR A LIQUID | |
| HYDROGEN STORAGE SYSTEM | 36 |
| Standard Test Method for Determining Gas Permeability | 36 |
| Permeability Apparatus | 37 |
| Specimen Description..... | 40 |
| Testing Procedure | 41 |
| Calculations | 41 |
| Calibration | 42 |
| Permeability Test Results | 43 |
| Optical Microscopic Analysis..... | 45 |
| RESULTS AND DISCUSSION | 49 |
| Micromechanics Method to Predict Thermal Stresses for Laminated Composites at | |
| Cryogenic Temperature | 49 |
| Fracture Toughness for a Transverse Crack in Laminated Composites at Cryogenic | |
| Temperatures..... | 50 |
| Permeability Testing for Laminated Composites for a Liquid Hydrogen Storage | |
| System..... | 50 |
| STRESS SINGULARITY USING STROH'S METHOD | 52 |
| LIST OF REFERENCES | 55 |

LIST OF TABLES

| <u>Table</u> | <u>page</u> |
|--|-------------|
| Table 2-1. Periodic boundary conditions for the square unit cell for unit values of different strain components. | 10 |
| Table 2-2. Periodic boundary conditions for the hexagonal unit cell for unit values of different strain components. | 10 |
| Table 2-3. Material properties of fibers used in the verification problem. | 12 |
| Table 2-4. Results of elastic constants for laminated composites calculated by empirical formulas. | 14 |
| Table 2-5. Results of elastic constants for laminated composite obtained by micromechanics analysis. | 15 |
| Table 2-6. Comparisons of G_{23} for square and hexagonal unit-cells in order to test transverse isotropy. | 15 |
| Table 2-7. Macro-strains in different laminates due to thermal loads ($\Delta T = -405$ K). The subscript Z denotes the thickness direction. | 18 |
| Table 2-8. Maximum principal stresses of a macro model for various graphite/epoxy composite systems. | 18 |
| Table 2-9. Maximum principal stresses in the fiber and matrix phases of a unit cell for various graphite/epoxy composite systems from micro-analysis. | 18 |
| Table 2-10. Percentage difference of principal stresses estimated by square and hexagonal unit cells. The negative sign indicates that micro-stress result estimated by the hexagonal unit cell is lower. | 18 |
| Table 2-11. Laminate macro-strains used to obtain the micro-stresses in the inner and outer face-sheets of the sandwich composite without internal pressure. | 22 |
| Table 2-12. Laminate macro-strains used to obtain the micro-stresses in the inner and outer face-sheets of the sandwich composite subjected to a pressure of 10 KPa. | 22 |
| Table 2-13. Maximum and minimum principal stresses in the fiber and matrix phases in the inner and outer face-sheets of the sandwich composite without internal pressure. | 23 |
| Table 2-14. Maximum and minimum principal stresses in the fiber and matrix phases in the inner and outer face-sheets of the sandwich composite subjected to a pressure of 10 KPa. | 23 |
| Table 3-1. Material properties of glass/epoxy and carbon/epoxy laminates. | 26 |
| Table 3-2. Singularity results of E-glass/epoxy. | 27 |
| Table 3-3. Singularity results of graphite/epoxy. | 27 |
| Table 3-4. Dimensions of specimens and various mid-ply thickness. | 30 |
| Table 3-5. Fracture load and fracture toughness at room and cryogenic temperatures. | 30 |
| Table 4-1. Molecular diameter of various gases from CRC Handbook of Chemistry and Physics, 54 th Edition. | 40 |
| Table 4-2. Description of composite specimens. | 40 |
| Table 4-3. Permeability of laminated composites for various number of cryogenic cycles. | 43 |
| Table 4-4. Permeability of textile composites for various number of cryogenic cycles. | 44 |
| Table 4-5. Permeability of laminated composites embedded with nano-particles for various number of cryogenic cycles. | 44 |

LIST OF FIGURES

| <u>Figure</u> | <u>page</u> |
|---|-------------|
| Figure 1-1. The X-33 test vehicle which NASA proposed as the replacement for the Space Shuttle. | 1 |
| Figure 1-2. Failure of sandwich composites used for the LH2 storage system. | 1 |
| Figure 1-3. Damage progression at cryogenic conditions. | 2 |
| Figure 1-4. SEM images of micro-crack propagation in composite laminates after thermo-mechanical cycles. | 4 |
| Figure 1-5. Variation of stresses acting normal to a crack tip, when the crack reaches a bi-material interface. | 5 |
| Figure 2-1. A square representative volume element and corresponding finite element mesh. | 9 |
| Figure 2-2. A hexagonal RVE and corresponding FE mesh. | 9 |
| Figure 2-3. Geometry of square and hexagonal unit cells. | 9 |
| Figure 2-4. Actual and average CTE of epoxy from curing temperature to cryogenic temperatures. | 11 |
| Figure 2-5. Young's modulus of epoxy as a function of temperature. | 12 |
| Figure 2-6. Longitudinal coefficient of thermal expansion with various fiber volume fractions for glass/epoxy and graphite/epoxy laminates. | 16 |
| Figure 2-7. Transverse coefficient of thermal expansion with various fiber volume fractions for glass/epoxy and graphite/epoxy laminates. | 16 |
| Figure 2-8. Flow chart of algorithm used to predict the failure due to micro-stresses. | 17 |
| Figure 2-9. Normal and shear stresses at the fiber-matrix interface in square and hexagonal unit cells. | 19 |
| Figure 2-10. Interfacial normal stresses in uniaxial graphite/epoxy laminate system at $\Delta T = -405$ K. | 20 |
| Figure 2-11. Interfacial shear stresses in uniaxial graphite/epoxy laminate system at $\Delta T = -405$ K. | 20 |
| Figure 2-12. Maximum principal stress distribution in the LH2 Graphite/Epoxy composite tank. Tank pressure = 10 KPa and temperature = 50 K ($\Delta T = -405$ K). .. | 21 |
| Figure 3-1. (a) Geometry of interfacial fracture specimens, (b) A crack normal to laminate interface with different stacking sequence. | 25 |
| Figure 3-2. Deformed geometry in the vicinity of a crack and interfacial fracture finite element model. | 26 |
| Figure 3-3. Contour plots of stress distribution for a $[0/90/0]_T$ composite model at a crack-tip under tensile and bending loads. | 26 |
| Figure 3-4. Stress distribution under (a) tensile loads; (b) bending loads. | 27 |
| Figure 3-5. Four-point bending test to determine the fracture load. | 28 |
| Figure 3-6. Load-displacement curves of four-point bending tests at room temperature for the Specimen 1. | 29 |
| Figure 3-7. Load-displacement curves of four-point bending tests at room temperature for the Specimen 2. | 29 |

| | |
|---|----|
| Figure 3-8. Load-displacement curves of four-point bending tests at room temperature for the Specimen 3 | 29 |
| Figure 3-9. Stress distribution for the 4-Pt bending simulation at (a) room temperature; (b) cryogenic temperature. | 30 |
| Figure 3-10. Variation of $\bar{K} = \sigma r^{\frac{1}{2}}$ with the distance from the crack tip at room temperature. | 31 |
| Figure 3-11. Logarithmic plot of the stresses as a function of distance from the crack-tip. | 31 |
| Figure 3-12. Cryogenic experimental setup of the four-point bending test. | 32 |
| Figure 3-13. Crack propagation in the 90° layer of a graphite/epoxy laminate at cryogenic temperature. | 32 |
| Figure 3-14. Contour plot of stresses normal to ply direction near the free-edge in a graphite/epoxy laminate at cryogenic temperature. | 33 |
| Figure 3-15. Load-displacement curves from four-point bending tests at cryogenic temperature. The mid-ply thickness and hence the specimen thickness varied from specimen to specimen. | 33 |
| Figure 3-16. Load-displacement curves from four-point bending tests at cryogenic temperature for the Specimen 1 | 34 |
| Figure 3-17. Load-displacement curves from four-point bending tests at cryogenic temperature for the Specimen 2 | 34 |
| Figure 3-18. Load-displacement curves from four-point bending tests at cryogenic temperature for the Specimen 3. | 34 |
| Figure 3-19. Variation of $\bar{K} = \sigma r^{\frac{1}{2}}$ with the distance from the crack tip at cryogenic temperature. | 35 |
| Figure 4-1. Permeability experimental setup for manometric determination method. | 36 |
| Figure 4-2. Permeability experimental setup for volumetric determination method. | 37 |
| Figure 4-3. Permeability testing apparatus. | 38 |
| Figure 4-4. Specimen installation between upstream and downstream chambers. | 39 |
| Figure 4-5. Variation of ambient pressure for 13 hours at test condition. | 42 |
| Figure 4-6. Variation of barometric pressure and indicator position as a function of time. | 43 |
| Figure 4-7. Logarithm of the permeability for composite specimens with increase of cryogenic cycles. | 45 |
| Figure 4-8. Cross sectional view of the graphite/epoxy composite specimen C2 before cryogenic cycling: (a) 10X magnification; (2) 40X magnification. | 46 |
| Figure 4-9. Microcrack propagation on the graphite/epoxy composite specimen C2 after cryogenic cycling: (a) 10X magnification; (2) 40X magnification. | 47 |
| Figure 4-10. Cross sectional view of the textile specimen T1 before cryogenic cycling, 10X magnification. | 47 |
| Figure 4-11. Microcrack propagation in the textile specimen T1 after cryogenic cycling: (a) 10X magnification; (b) 40X magnification. | 48 |
| Figure A.1. Geometry of an angle-ply laminated composite and a crack normal to an interface between two anisotropic materials. | 52 |

ABSTRACT

A micromechanics method is developed to investigate microcrack propagation in a liquid hydrogen composite tank at cryogenic temperature. The unit cell is modeled using square and hexagonal shapes depends on fiber and matrix layout from microscopic images of composite laminates. Periodic boundary conditions are applied to the unit cell. The temperature dependent properties are taken into account in the analysis. The laminate properties estimated by the micromechanics method are compared with empirical solutions using constituent properties. The micro stresses in the fiber and matrix phases based on boundary conditions in laminate level are calculated to predict the formation of microcracks in the matrix. The method is applied to an actual liquid hydrogen storage system. The analysis predicts micro stresses in the matrix phase are large enough to cause microcracks in the composite.

Stress singularity of a transverse crack normal to a ply-interface is investigated to predict the fracture behavior at cryogenic conditions using analytical and finite element analysis. When a transverse crack touches a ply-interface of a composite layer with same fiber orientation, the stress singularity is equal to $\frac{1}{2}$. When the transverse crack propagates to a stiffer layer normal to the ply-direction, the singularity becomes less than $\frac{1}{2}$ and vice versa. Finite element analysis is performed to predict the fracture toughness of a laminated beam subjected to fracture loads measured by four-point bending tests at room and cryogenic temperatures. As results, the fracture load at cryogenic temperature is significantly lower than that at room temperature. However, when thermal stresses are taken into consideration, for both cases of room and cryogenic temperatures, the difference of the fracture toughness becomes insignificant. The result indicates fracture toughness is a characteristic property, which is independent to temperature changes.

The experimental analysis is performed to investigate the effect of cryogenic cycling on permeability for various composite material systems. Textile composites have lower permeability than laminated composites even with increasing number of cryogenic cycle. Nano-particles dispersed in laminated composites do not show improvement on permeability. The optical inspection is performed to investigate the microcrack propagation and void content in laminated composites and compared the microscopic results before and after cryogenic cycling.

CHAPTER 1 INTRODUCTION

A composite material is made of two or more constituent materials to form a new material that is often superior in some respects to the constituents themselves. Composite materials offer many advantages, such as lightweight, high specific stiffness and specific strength, and low coefficient of thermal expansion. The next generation of reusable space launch vehicles is supposed to provide a 10-fold reduction in the cost of launching payloads into space, from \$10,000 to \$1,000 per pound in Figure 1-1.

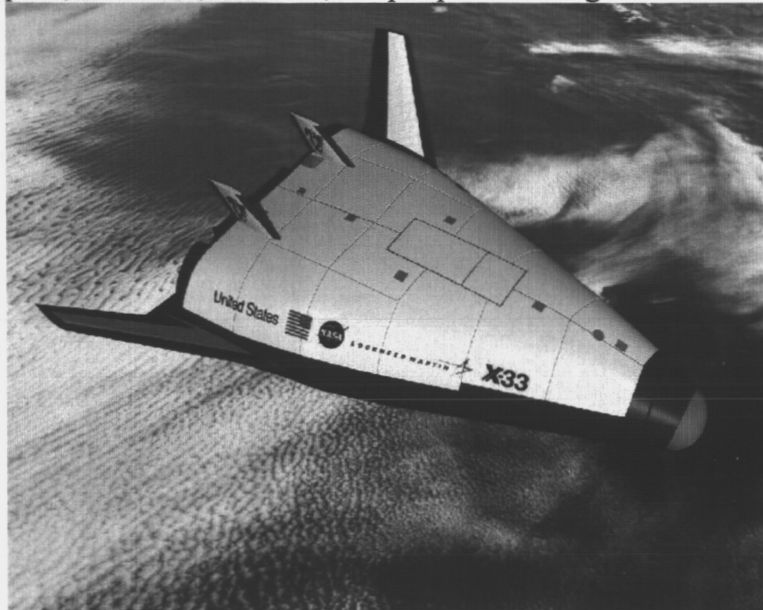


Figure 1-1. The X-33 test vehicle which NASA proposed as the replacement for the Space Shuttle.

Reducing the structure weight of the vehicle is of paramount importance in reducing the launch cost. Composite materials such as graphite/epoxy offer many advantages such as low density, high specific stiffness and specific strength, and low coefficient of thermal expansion. Therefore, fiber reinforced composite materials are candidate materials for cryogenic storage systems e.g., the liquid hydrogen (LH2) tank.

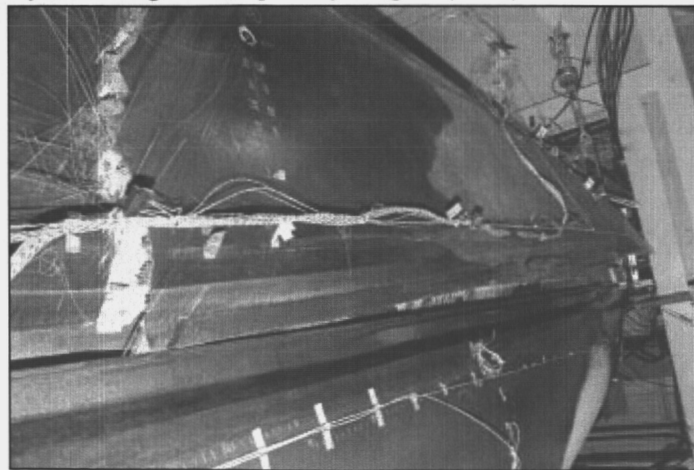


Figure 1-2. Failure of sandwich composites used for the LH2 storage system.

A previous design of the liquid hydrogen composite tank used composite sandwich structure made of graphite/epoxy composites and a honeycomb core. The composite tank is subjected to extremely low to high temperatures during and after re-entry into the atmosphere. During the proof test in November 1999 at NASA Marshall Space Flight Center, the composite liquid hydrogen tank failed because of microcrack propagation due to thermal stresses combined with mechanical loads (see Figure 1-2 [1]). Microcracks developed in the inner facesheet of the sandwich structure at cryogenic conditions. Then the microcracks, which usually develop in the transverse plies, can become delaminations. The delaminations connect the microcracks in adjacent layers and provide a leakage path for the cryogen. This can lead to catastrophic failure of the sandwich structure [1]. The failure motivates the present study on micromechanics analysis methods to predict microcracks in laminated composites.

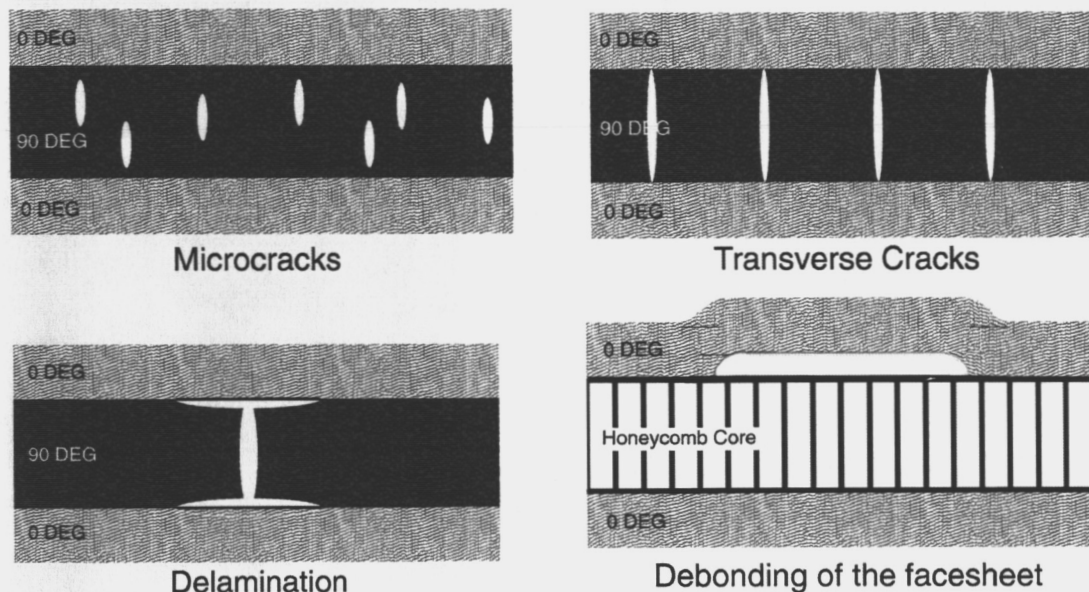


Figure 1-3. Damage progression at cryogenic conditions.

The damage progression of laminated composites at cryogenic temperatures is illustrated in Figure 1-3. At cryogenic temperatures, the microcracks initiate and propagate in laminated composites due to difference in thermal contraction between the fiber and matrix phases. When microcracks in the polymer matrix develop and reach the adjacent layers, the transverse cracks initiate. When the transverse crack develops further, the crack deflects through the interface between layers and delamination initiates. In the case of composite sandwich construction, debonding of the facesheet develops.

The purpose of this study is to investigate the possible causes of failure in laminated composites at cryogenic conditions. First, the micromechanics method is developed to predict the thermal stresses at microscale in fiber reinforced composites at cryogenic conditions. Second, fracture toughness of a transverse crack in composite laminates is evaluated to investigate the effect of cryogenic conditions on transverse crack propagation. Third, the permeability of various composite materials is evaluated to investigate the effect of cryogenic cycling on permeability.

Micromechanics Analysis of Laminated Composites at Cryogenic Conditions

From a macroscopic perspective, the composite material is considered to be homogeneous and transversely isotropic or orthotropic in general. For example, the laminated plate theory has been formulated based on this assumption. Even when three-dimensional analyses are used for composite structures, each ply or layer of the composite is modeled as a homogeneous orthotropic material. This macroscopic approximation has been found to be satisfactory in most analyses including thermal stress analyses. Thus most of the thermal stress problems in composites focus on the differences in thermal expansion coefficients between the plies. However, in extreme situations a micromechanics approach wherein the fiber and matrix phases are differentiated is necessary for accurate prediction of stresses, and hence failure. The present problem falls in this category. In order to predict the failure of a composite structure at the macroscopic scale, investigation of micromechanical behavior and understanding the failure mechanisms in the fibers and matrix at a micro-scale are necessary [2].

To make effective use of fiber-reinforced composites, we need a methodology to predict the thermo-mechanical properties at various temperatures as a function of fiber, matrix and interphase properties. These properties will be a strong function of temperature. Micromechanics is the study of such macroscopic properties from that of the constituent materials. In this study, micro-cracking behavior of the liquid hydrogen composite tank at cryogenic temperature is investigated using the micromechanics method. Failure of the composite tank under thermal and mechanical loads is evaluated by utilizing the commercial finite element software ABAQUS®. Also, the analysis is useful to develop a new composite material system for the liquid hydrogen composite tank by changing the combination of constituent properties.

Before finite element methods were widely available micromechanics analysis of fiber-reinforced composites was performed using analytical methods (e.g., Chen and Cheng [3]). They analyzed the unit cell of a composite by solving the governing elasticity equations using an infinite series and employing a combination of Fourier series and least square methods. The periodic boundary conditions for stresses and displacements were satisfied on symmetric boundaries. Micromechanics analysis methods for elastic-plastic composites were investigated using the bounding technique by Teply and Dvorak [4]. The problem of elastic-viscoplastic composites was solved by Paley and Aboudi [5] imposing continuity of traction and displacement rate at the interfaces between the constituents of a square unit cell. A square unit cell model was used by Nedele and Wisnom [6] to investigate the behavior of fiber-reinforced composites subjected to shear loading. Marrey and Sankar [7-9] developed micromechanics methods for textile structural composites using the finite element method. Their method considered the effects of stress gradients on the strength and stiffness properties of the composite. The periodic boundary condition of various shapes of unit cells was described by Li [10] using the symmetries of the fiber-matrix system to satisfy displacements and stresses in the boundary.

In the present study the micromechanics method is combined with a global laminate analysis to predict the stresses in the fiber and matrix phases accurately. The method is

useful to predict development of micro-cracks in a composite laminate at cryogenic temperatures. In order to predict the development of microcracks in fiber composites, one needs accurate description of the stresses in the matrix phase and also along the fiber-matrix interface. The problem of thermal stresses is complicated by the temperature dependent properties of the constituent materials. In the present study a global/local approach is used wherein traditional structural analysis is used to obtain information on macro-strains in a ply in the composite laminate. Then the macro-strains along with the local temperature are used in a micromechanical analysis to obtain detailed information on the stresses in the constituent phases. Two types of representative volume elements (RVE) are used in the micromechanical analyses. In the first one the RVE is a square with a circular fiber at the center of the square. In the second a hexagonal RVE is used. The differences in thermal stresses in the two RVE's are discussed. The temperature dependent properties of the matrix material are taken into account in the micromechanics. However, the fiber properties are assumed to be independent to temperature changes. The microstresses in different types of laminates used in a typical liquid hydrogen tank are studied and the possibility of micro-cracking is discussed. The results indicate that the maximum tensile stresses in the brittle matrix reach values very close to the tensile strength of the matrix material, raising the possibility of micro-crack development in composite liquid hydrogen storage systems.

Fracture Toughness of a Transverse Crack at Cryogenic Conditions

Microcracks develop in the facesheets of the sandwich structure due to the thermal cycling. The microcracks which usually develop in the transverse plies can propagate to an adjacent layer and become transverse cracks as shown in Figure 1-4. When the transverse crack deflects to the ply-interface, it becomes delaminations. The delaminations connect the microcracks in adjacent layers and provide a leakage path for the cryogen. For the liquid hydrogen composite tank, this hydrogen leakage through the interface sheet causes the catastrophic failure of the sandwich structure [1].

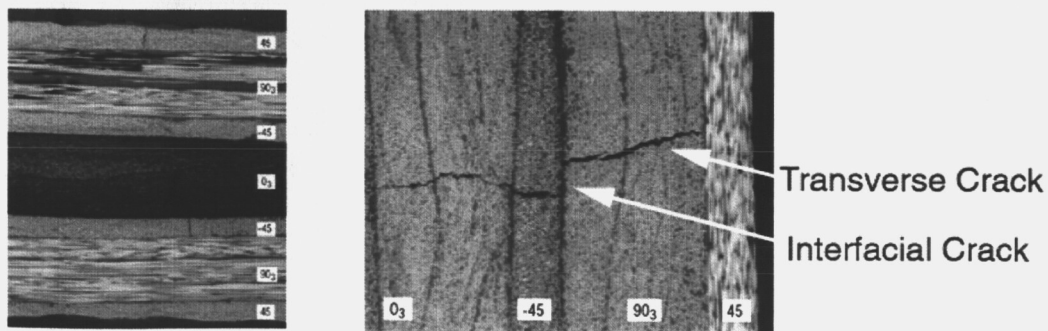


Figure 1-4. SEM images of micro-crack propagation in composite laminates after thermo-mechanical cycles.

When a microcrack propagates in a give material, the stress distribution normal to the crack plane can be described by the equation in Figure 1-5. Normal stresses at a crack-tip are governed by the stress singularity λ and stress intensity factor K_I . Zak and Williams [11] found the normal stresses ahead of a crack-tip are proportional to $r^{-\lambda}$ ($0 < \text{Re} [\lambda] < 1$) where r is the distance from the crack-tip. The stresses normal to the crack ahead of a

crack-tip can be expressed as $\sigma = K_I \cdot r^{-\lambda}$. The stress singularity of a micro-crack in laminated composites is governed by anisotropic properties at the vicinity of a crack-tip. The stress singularity describes the behavior of crack propagation. The Material 1 and the Material 2 are composite layers with specific fiber orientations. When a transverse crack reaches a ply-interface of composite layers with identical fiber orientation, stress singularity is equal to $\frac{1}{2}$ which is conventional singularity for homogeneous materials. When a transverse crack propagates from the Material 1 which is stiffer than the Material 2, the transverse crack penetrates the ply-interface and continues to propagate through the Material 2 until the crack reaches a stiffer layer [12]. In this case, the stress singularity becomes larger than $\frac{1}{2}$. When the Material 1 is softer than the Material 2, the transverse crack deflects to the ply-interface and becomes delamination. The stress singularity becomes lower than $\frac{1}{2}$. In this study, conditions under which a transverse crack becomes a delamination are studied, and the fracture toughness of the transverse crack is quantified and measured.

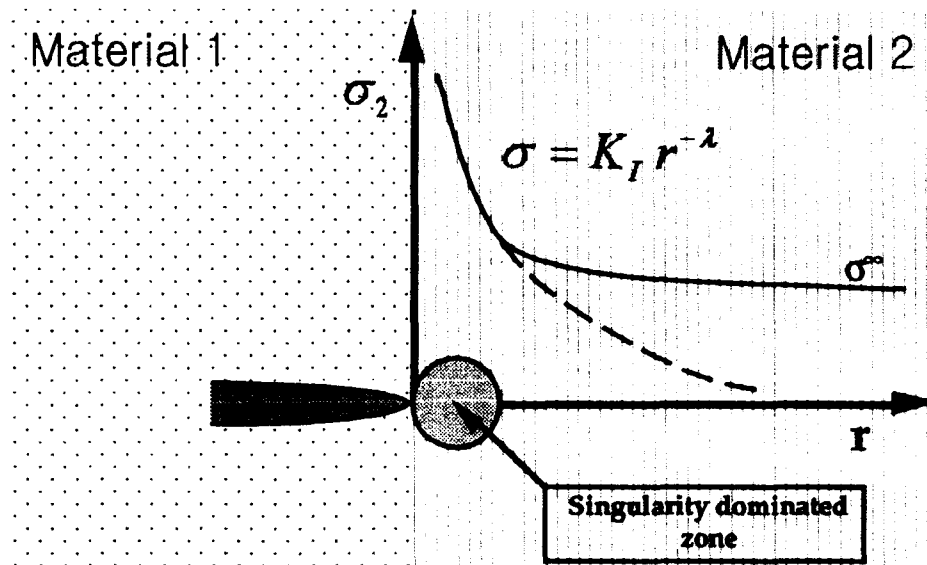


Figure 1-5. Variation of stresses acting normal to a crack tip, when the crack reaches a bi-material interface.

Williams [13] estimated the singularity for isotropic bi-material systems by solving a set of eigenfunctions developed by the continuity equations of normal and tangential stresses and displacements at the ply-interface. Ting and Chou [14] have developed methods to predict singularity at the free edge of a ply-interface of laminated composites. The general equations of displacement and stresses are derived in terms of arbitrary constants. The stress singularity is determined when the boundary condition at a crack plane and the continuity equations at the ply-interface are satisfied. Later, Ting and Hoang [15] developed this method to predict singularity of a transverse crack in laminated composites. Hutchinson and Suo [16] formulated a characteristic solution to predict stress singularity for isotropic bi-material in terms of Dundur's bimaterial parameters α and β . Gupta et al. [12] formulated a characteristic solution to predict the singularity for anisotropic bi-materials in terms of the bi-material parameters and individual material parameters. However, the characteristic equation is difficult to solve. In this study, stress

singularity of a transverse crack in a laminated composite is calculated using Ting's methods [14-15], and finite element analysis is used to compute the crack tip stress fields in various laminated composite models.

The purpose of the study is to develop the finite element model, which provides a confidence in capturing the stress singularity, and evaluate fracture toughness of a transverse crack in laminated composites at room and cryogenic temperatures. This study is useful to investigate the cryogenic effects on fracture toughness for composite laminates.

Permeability of Graphite Fiber Composite Materials at Cryogenic Conditions

Composite materials are good candidates for the liquid hydrogen storage tanks for space vehicles. A fundamental issue in composite tanks is hydrogen permeability, particularly since the failure of the liquid hydrogen composite tank could be caused by hydrogen leakage. Micro-cracking can also occur due to thermal and structural loads and fatigue. The liquid hydrogen storage composite tank is required to sustain large thermal and structural loads, and additionally must be able to endure several cycles of thermal loading without hydrogen permeation. The purpose of the study is to present the experimental work to measure the gas permeability of various types of composite systems.

The permeability testing on IM7/BMI laminated composites under bi-axial strains was performed by Stokes [17] following the ASTM Standard D-1434 [18]. The permeability was calculated by measuring the pressure difference across the specimen as a function of time. The permeability was measured as the strain was increased at room temperature. The permeability increase was steady until the specimen failed. Stokes found that the permeability is a time dependent parameter under constant strain condition. The crack densities for each layer were measured using microscopic optical inspection. The advantage of this test approach is that it minimizes the error due to the ambient pressure differences during the test. However, a precision pressure transducer is required to measure the accurate pressure difference across the specimen accurately.

The gas leakage through laminated composite was investigated by Kumazawa, et al [19] using experimental and finite element analysis. A finite element model with initial crack path was subjected to mechanical and thermal loads. The leakage rate decreased as temperatures decreased with assuming constant crack density. The FE results were compared with experimental results. Helium detector was used to measure the permeability of a laminated composite under biaxial loading.

The permeability test of hybrid composites and related films was performed by Grimsley et al [20] following the ASTM Standard D-1434. The volume-flow rate was estimated by measuring the rate of moving distance of a liquid indicator in a glass capillary tube. The gas transmission rate is converted to volume-flow rate using the ideal gas law. The permeance is calculated by the gas transmission rate per upstream pressure. The permeability results for various types of hybrid composites and films were provided. Also, Herring [21] investigated the permeability of thin film polymers after pre-conditioning samples. The permeability is calculated according to ASTM D-1434.

The volumetric method to calculate the permeability is verified by Nettles [22]. The study is to investigate the effect on permeability test of laminated composites after experiencing impact loads. Moreover, the study investigated the possible cases of testing condition, which influence the permeability results. When the glass capillary tube is mounted vertically or horizontally, the variation of permeability results is insignificant. The permeability tests were performed using various types of liquid indicators in a capillary tube. The variation of permeability results was found to be insignificant. Also, the length of liquid indicator does not affect the permeability results. However, the glass capillary tube with inner diameter 0.4 mm underestimated permeability than the capillary tubes with 1.2 mm and 3 mm diameters.

The permeability test on laminated composites and bonding materials were performed by Nettles [23]. The permeability results before and after cryogenic cycles were compared. The composite specimens of both type of prepreg materials and layup configuration have low permeation results after 4 and 12 cryogenic cycles. Glass et al. investigated the permeability for core materials of a composite sandwich when it is subjected to shear loads [24]. The Hexcel HRP honeycomb and the Dupont Korex honeycomb were chosen for core materials. The composite sandwich specimens were fabricated and air inlet holes were drilled through a facesheet. The permeability is calculated by measuring the flow rate of upstream air.

In this study, the permeability was estimated for various composite material systems as the composite laminates undergo cryogenic cycling. An optical microscope was used to understand the nature of microcrack propagation after cryogenic cycling. The permeability increased rapidly and became constant as the number of cryogenic cycles increased. The permeability is proportional to the crack density since increasing number of cracks produces a larger flow path though the thickness of the material. The optical inspection on composite specimens was performed to investigate the behavior of microcrack propagation after cryogenic cycling. The optical results were compared before and after cryogenic cycling on various composite specimens.

CHAPTER 2

MICROMECHANICS METHODS TO PREDICT MICRO-STRESSES IN LAMINATED COMPOSITES AT CRYOGENIC TEMPERATURES

A finite element analysis based micromechanics method is developed to investigate development of micro-cracks in a graphite/epoxy composite liquid hydrogen tank at cryogenic temperatures. The unit-cell of the composite is modeled using finite elements. Periodic boundary conditions are applied to the boundaries of the unit-cell. The temperature dependent properties including the coefficient of thermal expansion of the matrix material is taken into account in the analysis. The thermo-elastic constants of the composite were calculated as a function of temperature. The stresses in the fiber and matrix phases and along the fiber-matrix interface were calculated. When the laminated composite structure is subjected to combined thermal and mechanical loads, the macro-strains are computed from the global analysis. Then, the macro-strains and temperatures are applied to the unit cell model to evaluate micro-stresses, which are used to predict the formation of micro-cracks in the matrix. The method is applied to a composite liquid hydrogen storage system. It is found that the stresses in the matrix phase could be large enough to cause micro-cracks in the composite.

Micromechanics Model

The microscopic image of a uniaxial fiber reinforced laminate (Figures 2-1 and 2.2) shows that the fiber arrangement is quite random in reality. However, for analytical/numerical modeling, it is convenient to assume some repetitive pattern of fiber arrangement. The square unit cell is not a suitable model for glass, carbon, and graphite fibers since the model is not transversely isotropic but tetragonal. The square array is conceivable applicable to boron/aluminum composites in which fibers are arranged in patterns that resemble such arrays. However, it is not applicable to any type of boron tapes or preregs. The reason is that these are thin unidirectionally reinforced layers whose thickness is of the order of the diameter of one boron fiber and can not be consider composite materials.

The unit cell is modeled from the repetitive pattern of the fiber and matrix layout of composite laminates. In the present analysis, both square and hexagonal unit cells are considered for the micromechanics model. In both cases the dimensions are chosen such that the fiber volume ratio is 60%, which is typical of graphite/epoxy composites. When fibers are arranged in a square unit cell one can obtain a maximum fiber volume fraction of 79%. The square unit cell was modeled using 1,600 quadratic solid elements with periodic boundary conditions [7-9]. The periodic boundary conditions ensure displacement compatibility and stress continuity on the opposite faces of the unit-cell.

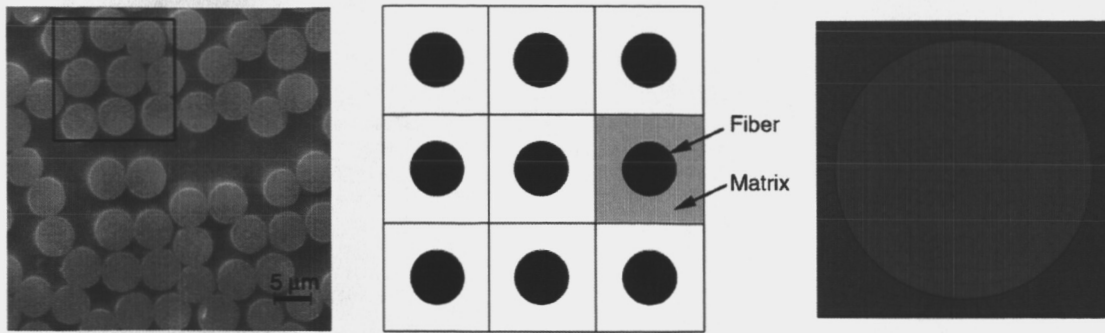


Figure 2-1. A square representative volume element and corresponding finite element mesh.

The hexagonal pattern of unit cell can be found more commonly in fiber-matrix composites, especially when the composite is fabricated with high fiber volume fraction. Theoretically one can obtain a maximum fiber volume fraction of 91% with hexagonal RVE. In a hexagonal RVE there is symmetry about the y -axis and also about the ± 30 degree directions. The hexagonal unit cell is modeled using 2,400 quadratic solid elements with periodic boundary conditions [10].

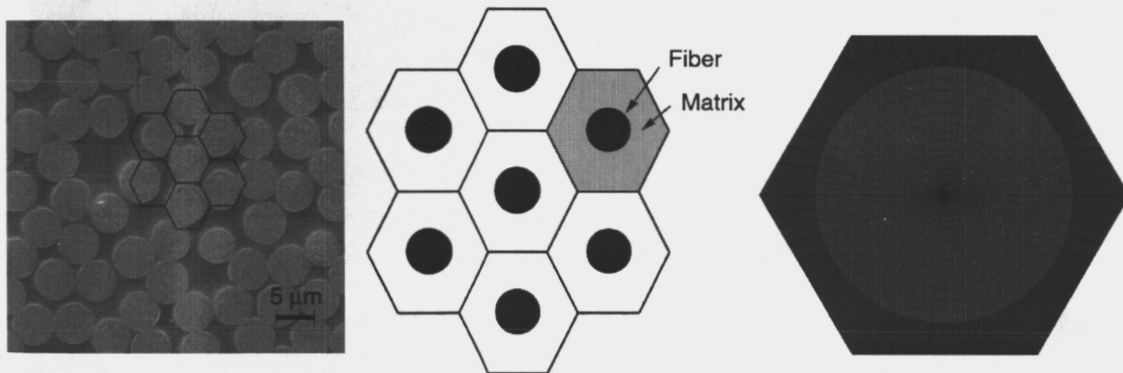


Figure 2-2. A hexagonal RVE and corresponding FE mesh.

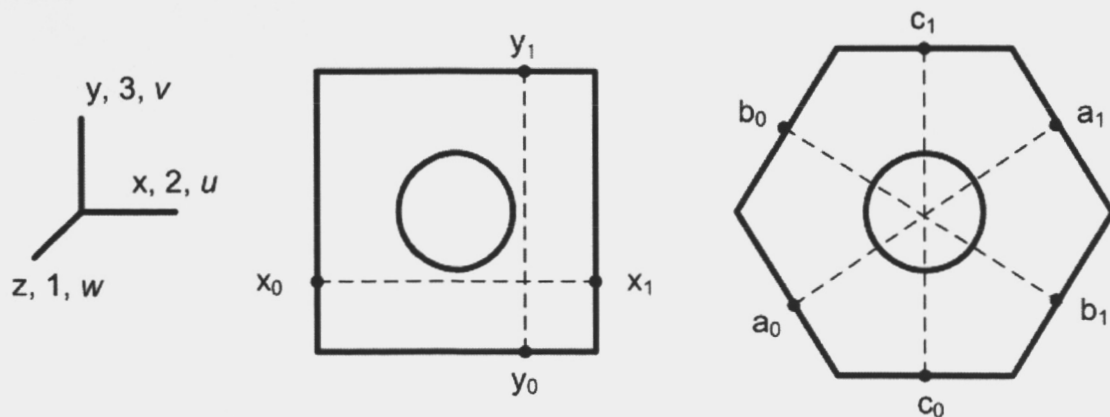


Figure 2-3. Geometry of square and hexagonal unit cells.

The unit cells are subjected to axial and shear displacements combined with thermal effects using periodic boundary conditions. The boundary condition on a RVE element is established by symmetry consideration so that the micromechanics analysis can be

confined to a single repeating element. The periodic boundary conditions maintain equal boundary displacements with the adjacent unit cells to satisfy the compatibility of displacements on opposite faces of the unit cell and enforce the continuity of stresses. The unit-cell is subjected to different strain components individually using the periodic boundary conditions shown in Table 2-1 [7-9]. For the hexagonal unit cell, the periodic boundary conditions corresponding to unit value of each strain component are shown in Table 2-2 [10]. The equations of periodic boundary conditions corresponding individual unit strains were embedded in the ABAQUS[®] input code to perform the finite element (FE) analysis.

Table 2-1. Periodic boundary conditions for the square unit cell for unit values of different strain components.

| $\varepsilon_x=1$ | $\varepsilon_y=1$ | $\varepsilon_z=1$ | $\gamma_{xy}=1$ | $\gamma_{xz}=1$ | $\gamma_{yz}=1$ |
|-------------------|-------------------|-------------------|------------------------------|-------------------|-------------------|
| $u_{x1}-u_{x0}=L$ | $u_{x1}-u_{x0}=0$ | $u_{x1}-u_{x0}=0$ | $v_{x1}-v_{x0}=\frac{1}{2}L$ | $w_{x1}-w_{x0}=L$ | $w_{y1}-w_{y0}=L$ |
| $v_{y1}-v_{y0}=0$ | $v_{y1}-v_{y0}=L$ | $v_{y1}-v_{y0}=0$ | $u_{y1}-u_{y0}=\frac{1}{2}L$ | $u_{z1}-u_{z0}=0$ | $v_{z1}-v_{z0}=0$ |
| $w_{z1}-w_{z0}=0$ | $w_{z1}-w_{z0}=0$ | $w_{z1}-w_{z0}=t$ | $w_{z1}-w_{z0}=0$ | | |

Table 2-2. Periodic boundary conditions for the hexagonal unit cell for unit values of different strain components.

| $\varepsilon_x=1$ | $\varepsilon_y=1$ | $\varepsilon_z=1$ | $\gamma_{xy}=1$ | $\gamma_{xz}=1$ | $\gamma_{yz}=1$ |
|-------------------------------------|------------------------------|-------------------|--------------------------------------|-------------------------------------|------------------------------|
| $u_{a1}-u_{a0}=\frac{\sqrt{3}}{2}L$ | $u_{a1}-u_{a0}=0$ | $u_{a1}-u_{a0}=0$ | $u_{a1}-u_{a0}=0$ | $u_{z1}-u_{z0}=0$ | $v_{z1}-v_{z0}=0$ |
| $u_{b1}-u_{b0}=\frac{\sqrt{3}}{2}L$ | $u_{b1}-u_{b0}=0$ | $u_{b1}-u_{b0}=0$ | $u_{b1}-u_{b0}=0$ | $u_{c1}=0$ | $w_{c1}=\frac{1}{2}L$ |
| $u_{c1}-u_{c0}=0$ | $v_{a1}-v_{a0}=\frac{1}{2}L$ | $v_{a1}-v_{a0}=0$ | $u_{c1}=0$ | $u_{c0}=0$ | $w_{c0}=-\frac{1}{2}L$ |
| $v_{b1}-v_{b0}=0$ | $v_{b1}-v_{b0}=\frac{1}{2}L$ | $v_{b1}-v_{b0}=0$ | $u_{c0}=0$ | $v_{c1}=0$ | $w_{a1}-w_{a0}=\frac{1}{2}L$ |
| $v_{c1}=0$ | $v_{c1}=\frac{1}{2}L$ | $v_{c1}=0$ | $v_{a1}-v_{a0}=\frac{\sqrt{3}}{2}L$ | $v_{c0}=0$ | $w_{b0}-w_{b1}=\frac{1}{2}L$ |
| $v_{c0}=0$ | $v_{c0}=-\frac{1}{2}L$ | $v_{c0}=0$ | $v_{b1}-v_{b0}=-\frac{\sqrt{3}}{2}L$ | $w_{a1}-w_{a0}=\frac{\sqrt{3}}{2}L$ | |
| $w_{z1}-w_{z0}=0$ | $w_{z1}-w_{z0}=0$ | $w_{z1}-w_{z0}=t$ | $w_{z1}-w_{z0}=0$ | $w_{b1}-w_{b0}=\frac{\sqrt{3}}{2}L$ | |

Thermo-Elastic Properties of the Composite Constituents

For accurate prediction of stresses at cryogenic conditions, one requires temperature dependent thermo-elastic properties of the constituent materials. In the present study the matrix properties are considered as temperature-dependent and the fiber properties temperature independent. Most of the advanced composite systems such as aerospace graphite/epoxy are cured at about 455 K. When the temperature rises above the melting temperature T_m , the epoxy resin becomes a rubbery solid and then becomes viscous liquid. When the laminate is cooled down to the glass transition temperature T_g , the epoxy resin becomes an amorphous solid. The difference in the coefficients of thermal expansion (CTE) for the constituents under temperature changes causes residual stresses in the composite laminate. Thermal stresses in composites are largely influenced by matrix thermo-mechanical properties. Also, the chemical reaction of epoxy causes shrinkage which rises residual stress in matrix phase. In this study, the residual stress due to chemical reaction of epoxy is assumed to be negligible.

In this study, the 977-3 epoxy system is used as the matrix material. The coefficient of thermal expansion and the Young's modulus of this material system [25] as a function of temperature are shown in Figures 2-4 and 2-5, respectively. The actual and average CTE of the epoxy resin are nonlinear with respect to temperature as shown in Figure 2-4. The average CTE from a reference temperature is used as input in the ABAQUS® finite element program. The average CTE is calculated by using the relation

$$\bar{\alpha} = \frac{\int_{T_{Curing}}^{T_{Cryogenic}} \alpha(T) dT}{T - T_{Curing}} \quad (2.1)$$

In the above equation, the curing temperature T_{curing} is 455K where the epoxy resin becomes solid during curing process of composite laminates. The cryogenic temperature $T_{cryogenic}$ is 50K where the liquid hydrogen boils.

When the temperature decreases from curing to cryogenic temperature, the actual CTE decreases from $73.0 \times 10^{-6}/K$ to $18.1 \times 10^{-6}/K$ and the Young's moduli increases from 1.2 MPa to 5.2 MPa. The tensile strength for heat-cured epoxy is in the range of 70 MPa to 90 MPa at room temperature [26]. In general, the strength of epoxy increases from curing to cryogenic temperature since the epoxy becomes brittle [25], but no data is available in the complete range of temperatures up to liquid hydrogen temperature. In this study, the tensile strength of the epoxy is assumed as 100 MPa at cryogenic temperature.

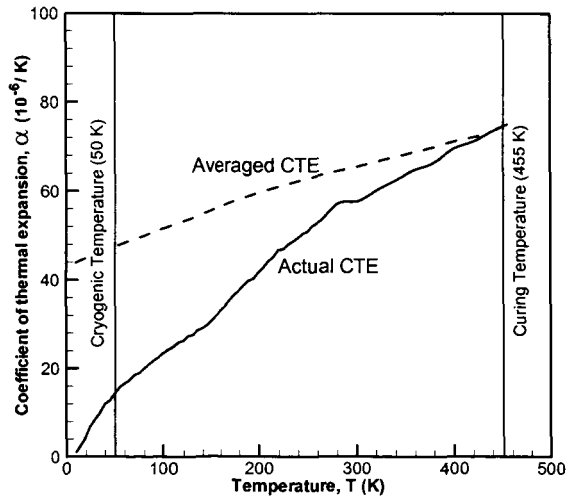


Figure 2-4. Actual and average CTE of epoxy from curing temperature to cryogenic temperatures.

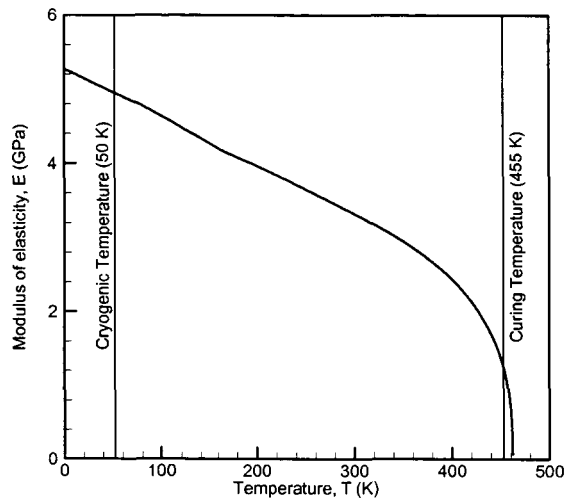


Figure 2-5. Young's modulus of epoxy as a function of temperature.

Table 2-3. Material properties of fibers used in the verification problem.

| | E-Glass Fiber | Graphite Fiber (IM7) |
|--|---------------|----------------------|
| E_1 (GPa) | 72.4 | 263 |
| E_2, E_3 (GPa) | 72.4 | 19 |
| G_{12}, G_{13} (GPa) | 30.2 | 27.6 |
| G_{23} (GPa) | 30.2 | 27.6 |
| ν_{12}, ν_{13} | 0.2 | 0.2 |
| ν_{23} | 0.2 | 0.35 |
| α_{11} ($10^{-6}/C^{\circ}$) | 5.0 | -0.9 |
| α_{22}, α_{33} ($10^{-6}/C^{\circ}$) | 5.0 | 7.2 |
| Tensile strength (MPa) | 1,104 | 1,725 |

The transversely isotropic properties of the glass and graphite fibers used in this study are shown in Table 2-3 [26-27]. The material properties of fiber are assumed to be independent to temperature changes.

Estimation of Thermo-Elastic Constants

The properties of a composite material depend on the constituent properties and the microstructure of fiber and matrix layout and can be estimated by experimental analysis and theoretical solutions. The experimental analysis is simple and trustworthy but time consuming and expensive. Since the results are variable to fiber volume fraction, constituent properties and fabrication process, the experimental analysis is required to repeat the testing procedures. The theoretical and semi-empirical methods can be effective when the composite material involves many variables which can affect composite properties. However, the methods may not be reliable for component design purpose and present difficulty in selecting a representative but tractable mathematical model for some cases such as the transverse properties of some of the unidirectional composites [26]. The mathematical solutions are unavailable as a simple form to predict

the transverse properties such as shear moduli G_{23} and Poisson's ratio ν_{23} [26]. In this study, the micromechanics method is performed to estimate the laminate properties of various laminate systems and compared with theoretical and semi-empirical solutions to verify the transverse isotropy.

The unit cell model is used to estimate the elastic constants and the coefficient of thermal expansion using the FE based micromechanics method. The fiber volume fraction was assumed to be 60%. The thermo-elastic stress-strain relations of the composite material at macro-scale can be written as

$$\begin{Bmatrix} \sigma_1 \\ \sigma_2 \\ \sigma_3 \\ \tau_{23} \\ \tau_{31} \\ \tau_{12} \end{Bmatrix} = \begin{bmatrix} C_{11} & C_{12} & C_{13} & 0 & 0 & 0 \\ & C_{22} & C_{23} & 0 & 0 & 0 \\ & & C_{33} & 0 & 0 & 0 \\ & & & C_{44} & 0 & 0 \\ & SYM & & & C_{55} & 0 \\ & & & & & C_{66} \end{bmatrix} \begin{Bmatrix} \varepsilon_1 \\ \varepsilon_2 \\ \varepsilon_3 \\ \gamma_{23} \\ \gamma_{31} \\ \gamma_{12} \end{Bmatrix} - \Delta T \begin{Bmatrix} \alpha_1 \\ \alpha_2 \\ \alpha_3 \\ \alpha_{23} \\ \alpha_{31} \\ \alpha_{12} \end{Bmatrix} \quad (2.2)$$

The elastic constants and the CTE's in Equation 2.2 were obtained by performing 7 sets of micromechanical analyses. In the first 6 cases the temperature difference ΔT was set to zero and the unit-cell was subjected to periodic boundary conditions corresponding to one of the macro-strains as given in Tables 1 and 2. The macro-stresses in the unit cell were calculated as the volume average of the corresponding micro-stress components:

$$\sigma_i = \frac{1}{V} \sum_{k=1}^{NELM} \sigma_i^{(k)} V^{(k)}, \quad i = 1, 6 \quad (2.3)$$

In Equation 2.3, k denotes the element number, $NELM$ is the total number of elements in the FE model, $V^{(k)}$ is the volume of the k^{th} element and V is the volume of the unit-cell. The average or macro-stresses are used to calculate the stiffness coefficients in a column corresponding to the nonzero strain. In order to calculate the CTE's, the unit-cell is subjected to periodic boundary conditions such that the macro-strains are identically equal to zero and a uniform ΔT is applied to the unit-cell. From the macro-stresses the CTE's can be calculated as

$$\{\alpha\} = \frac{1}{\Delta T} [C]^{-1} \{\sigma\} \quad (2.4)$$

In this study the properties and residual stresses were calculated at 50 K which corresponds to $\Delta T = -405$ K. The elastic constants such as Young's moduli, shear moduli and Poisson's ratios can be obtained from the compliance matrix $S = C^{-1}$.

Table 2-4. Results of elastic constants for laminated composites calculated by empirical formulas.

| | Elastic constants | Empirical Formulas (EMP) |
|----------------|--|--------------------------|
| Glass/Epoxy | E_1 (GPa) | 45.4 |
| | E_2, E_3 (GPa) | 19.4 |
| | G_{12}, G_{13} (GPa) | 6.00 |
| | G_{23} (GPa) | 7.71 |
| | ν_{12}, ν_{13} | 0.260 |
| | ν_{23} | 0.255 |
| | α_1 ($10^{-6}/C^{\circ}$) | 5.41 |
| | α_2, α_3 ($10^{-6}/C^{\circ}$) | 9.92 |
| Graphite/Epoxy | E_1 (GPa) | 160 |
| | E_2, E_3 (GPa) | 11.1 |
| | G_{12}, G_{13} (GPa) | 5.90 |
| | G_{23} (GPa) | 4.05 |
| | ν_{12}, ν_{13} | 0.260 |
| | ν_{23} | 0.367 |
| | α_1 ($10^{-6}/C^{\circ}$) | -0.712 |
| | α_2, α_3 ($10^{-6}/C^{\circ}$) | 12.1 |

The empirical formulas are used to estimate the elastic constant based on constituent properties as shown in Table 2-4. The rule of mixture is used to calculate the approximate elastic constant E_1 , ν_{12} and ν_{13} . Halpin-Tsai [26] equations are used to calculate the approximate elastic constants $E_2, E_3, G_{12}, G_{13}, G_{23}$ and ν_{23} . Schaprey's formulas [26] are used for the coefficient of thermal expansion α_1, α_2 and α_3 . The thermo-elastic constants determined from the micromechanical analyses are compared with available empirical formulas in Table 2-5. The results from the FE model and the empirical formulas (EMP) agree reasonably well. The elastic moduli E_1 and E_2 from the FE models and the empirical formulas differ by less than 4%. However, the transverse modulus is very sensitive to the geometry of the unit cell. Since Halpin-Tsai equations are empirical, the method cannot accurately predict the transverse modulus. There are no simple solutions to estimate the elastic properties G_{23} and ν_{23} [26]. In present study, the properties G_{23} and ν_{23} are estimated by the Halpin-Tsai [26] equations and the difference is comparatively larger than other results.

Table 2-5. Results of elastic constants for laminated composite obtained by micromechanics analysis.

| | Elastic constants | Square Unit Cell (SQR) | | Hexagonal Unit Cell (HEX) | | Difference between SQR and HEX (%) |
|------------------------|--|------------------------|-----------------------------------|---------------------------|------------------------------------|------------------------------------|
| | | FE Result | Difference between SQR and EMP(%) | FE Result | Difference between HEX and EMP (%) | |
| Glass/ Epoxy | E_1 (GPa) | 45.4 | 0.13 | 45.5 | 0.13 | 0.26 |
| | E_2, E_3 (GPa) | 19.7 | 2.02 | 16.3 | 18.5 | 17.3 |
| | G_{12}, G_{13} (GPa) | 6.10 | 1.60 | 5.59 | 7.31 | 8.30 |
| | G_{23} (GPa) | 4.62 | 66.8 | 5.83 | 32.2 | 26.1 |
| | ν_{12}, ν_{13} | 0.253 | 2.83 | 0.260 | 0.08 | 2.91 |
| | ν_{23} | 0.275 | 7.35 | 0.391 | 33.1 | 38.5 |
| | α_1 ($10^{-6}/C^{\circ}$) | 5.45 | 0.75 | 5.46 | 0.91 | 0.16 |
| | α_2, α_3 ($10^{-6}/C^{\circ}$) | 9.04 | 9.75 | 9.27 | 7.03 | 2.54 |
| Graphite / Epoxy | E_1 (GPa) | 159 | 0.43 | 160 | 0.10 | 0.33 |
| | E_2, E_3 (GPa) | 11.5 | 3.75 | 10.8 | 2.31 | 5.92 |
| | G_{12}, G_{13} (GPa) | 5.98 | 1.41 | 5.50 | 7.17 | 8.01 |
| | G_{23} (GPa) | 3.40 | 19.0 | 3.72 | 8.99 | 9.20 |
| | ν_{12}, ν_{13} | 0.257 | 1.29 | 0.254 | 2.29 | 0.98 |
| | ν_{23} | 0.417 | 12.1 | 0.448 | 18.1 | 7.37 |
| | α_1 ($10^{-6}/C^{\circ}$) | -0.698 | 2.00 | -0.685 | 3.94 | 1.86 |
| | α_2, α_3 ($10^{-6}/C^{\circ}$) | 11.6 | 4.91 | 11.6 | 4.17 | 0.71 |

To verify the transverse isotropy of the square and hexagonal unit cells, the shear modulus G_{23} calculated from the transverse Young's modulus and Poisson's ratio is compared with the G_{23} calculated using the results from the FE analysis. If the composite is truly transversely isotropic, then it should satisfy the relation $G_{23} = \frac{E_2}{2(1+\nu_{23})}$. As shown in

Table 2-6, the difference in the shear moduli calculated from the two methods is small for the hexagonal unit-cell. Therefore, the hexagonal unit cell is a better model for the micromechanics model to satisfy the transverse isotropy and can be considered as more realistic for fiber-reinforced composites [28]. Also, the results the micromechanics method provides better approximate results of laminate properties than empirical solutions.

Table 2-6. Comparisons of G_{23} for square and hexagonal unit-cells in order to test transverse isotropy.

| | Square Cell (MPa) | | | Hexagonal Cell (MPa) | | |
|----------------|-------------------|--------------------------------|---------|----------------------|--------------------------------|---------|
| | G_{23} | $\frac{E_{23}}{2(1+\nu_{23})}$ | % Error | G_{23} | $\frac{E_{23}}{2(1+\nu_{23})}$ | % Error |
| Glass/Epoxy | 4.62 | 7.74 | 67.5 | 5.83 | 5.91 | 1.41 |
| Graphite/Epoxy | 3.40 | 4.06 | 19.3 | 3.72 | 3.74 | 0.56 |

Effects of Fiber Volume Fraction

The effect of fiber volume fraction on the thermal coefficients of graphite/epoxy composite was analyzed using the micromechanics method. Figures 2-6 and 2-7 show the variation of longitudinal and transverse thermal coefficients as a function of fiber volume fraction for glass/epoxy and graphite/epoxy composites. The CTE's estimated using both square and hexagonal unit-cells are very close. It should be noted that the graphite fiber has a negative thermal coefficient, and also the product of thermal coefficient α and Young's modulus (αE) is almost equal for the fiber and matrix. Hence the longitudinal thermal coefficients are negligibly small and it changes sign as the fiber volume fraction is varied. At about 40% fiber volume fraction the longitudinal thermal coefficient is almost equal to zero. The transverse thermal coefficient also reduces due to increase in fiber volume fraction because of the reduction in the effect of matrix material. The results show the micromechanics method is useful to develop composite materials for various applications by changing the combination of the constituent materials.

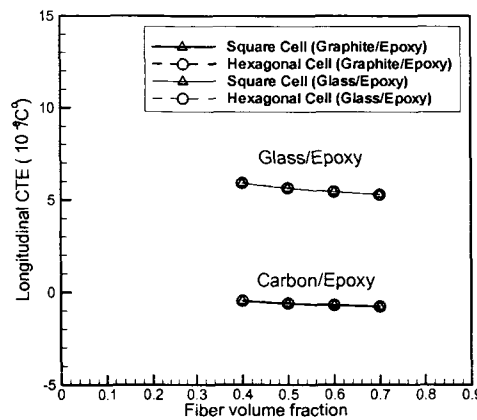


Figure 2-6. Longitudinal coefficient of thermal expansion with various fiber volume fractions for glass/epoxy and graphite/epoxy laminates.

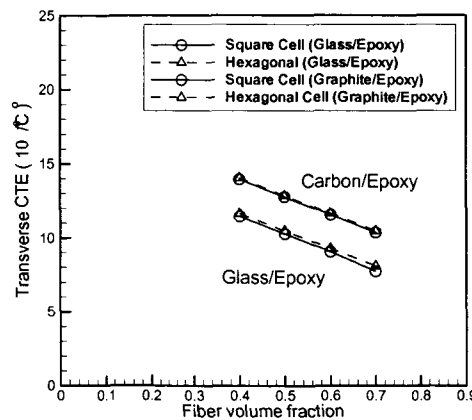


Figure 2-7. Transverse coefficient of thermal expansion with various fiber volume fractions for glass/epoxy and graphite/epoxy laminates.

Prediction of Stresses at Microscopic Level

The micromechanics method was extended to estimate the micro-stresses of the graphite/epoxy composite laminate under combined thermal and external loads. The procedure used to obtain the relation between macro- and micro- stresses is described in the algorithm shown in Figure 2-8. Six independent sets of unit strains are applied to the unit cell boundary as explained in the previous section and micro-stresses are calculated in each element corresponding to the unit strain states. The temperature in the unit-cell was also made equal to the temperature of the structure. The individual micro-stresses are multiplied by laminate strains in each layer calculated using the laminate theory [26].

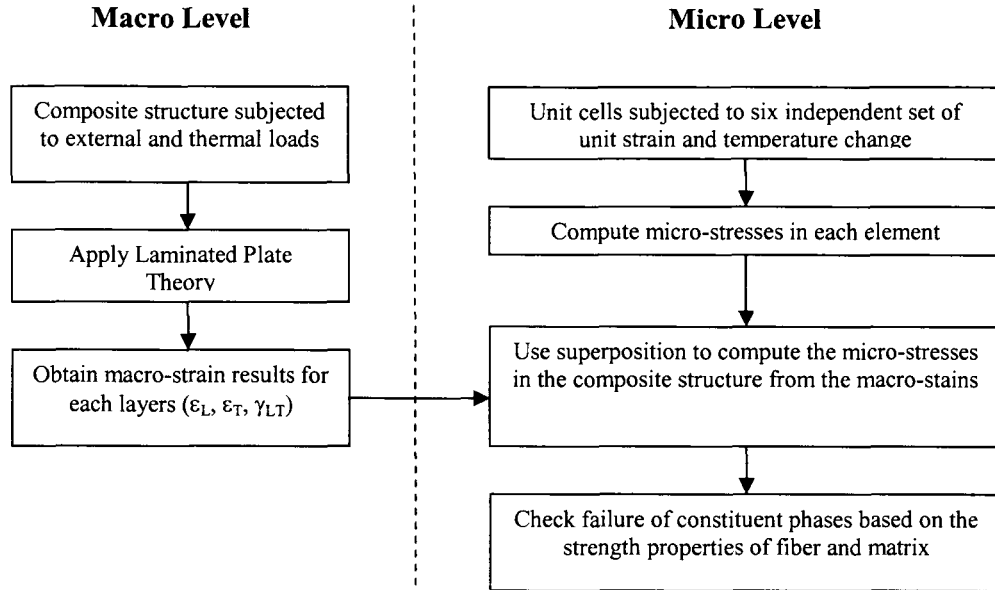


Figure 2-8. Flow chart of algorithm used to predict the failure due to micro-stresses.

The micro-stresses obtained by superposition are used to calculate the maximum and minimum stresses in each finite element in the unit-cell model. The failure of laminate can be predicted by using the maximum stress criterion for the fiber and matrix phases. The maximum stress criterion is reasonable as the fiber and matrix are expected to behave in a brittle manner at cryogenic temperature. The tensile strength of graphite fibers is taken as 1,725 MPa and that of epoxy at cryogenic temperature is approximately 100 MPa.

The analysis is performed to estimate the micro-stresses of the graphite/epoxy composite laminates (IM7/977-3) with various stacking sequence (Sample A: $[0]_s$; Sample B: $[0/\overline{90}]_s$ and Sample C: $[0/45/\overline{90}]_s$) when it is subjected to thermal stresses at cryogenic temperatures without external loads. The thickness for each layer of the specimens is 0.07 mm. For the various laminated specimens, the longitudinal and transverse strains at the laminate level at cryogenic temperature ($\Delta T = -405$ K) were calculated using the laminate theory and they are presented in Table 2-7. The micro level stresses were obtained by superposition principle as described above. In the case of plane-stress normal to the laminate plane, the strain in thickness direction can be calculated by

$$\varepsilon_3 = \frac{-C_{31}(\varepsilon_1 - \alpha_1 \Delta T) - C_{32}(\varepsilon_2 - \alpha_2 \Delta T)}{C_{33}} + \alpha_3 \Delta T \quad (5)$$

Table 2-7. Macro-strains in different laminates due to thermal loads ($\Delta T = -405$ K). The subscript Z denotes the thickness direction.

| Sample | θ | $\epsilon_L (10^{-3})$ | $\epsilon_T (10^{-3})$ | $\epsilon_Z (10^{-3})$ | $\gamma_{LT} (10^{-3})$ | $\gamma_{LZ} (10^{-3})$ | $\gamma_{TZ} (10^{-3})$ |
|--------|----------|------------------------|------------------------|------------------------|-------------------------|-------------------------|-------------------------|
| A | 0 | 0.277 | -4.71 | -4.71 | 0 | 0 | 0 |
| | 0 | 0.0476 | -0.382 | -6.59 | 0 | 0 | 0 |
| B | 90 | -0.382 | 0.0476 | -6.63 | 0 | 0 | 0 |
| | 0 | -0.130 | -0.648 | -6.406 | 1.410 | 0 | 0 |
| C | 45 | 0.316 | -1.094 | -6.369 | -0.518 | 0 | 0 |
| | 90 | -0.648 | -0.130 | -6.449 | -1.410 | 0 | 0 |

Table 2-8. Maximum principal stresses of a macro model for various graphite/epoxy composite systems.

| Sample | Orientation, θ | Laminate Plate Theory | | |
|--------|-----------------------|-----------------------|------------------|---------------------|
| | | σ_L (MPa) | σ_T (MPa) | γ_{LT} (MPa) |
| A | 0 | 0 | 0 | 0 |
| | 0 | -24.9 | 46.4 | 0 |
| B | 90 | -92.9 | 49.9 | 0 |
| | 0 | -54.3 | 43.1 | 7.76 |
| C | 45 | 16.2 | 39.5 | -2.85 |
| | 90 | -136 | 47.3 | -7.76 |

Table 2-9. Maximum principal stresses in the fiber and matrix phases of a unit cell for various graphite/epoxy composite systems from micro-analysis.

| Sample | θ | Square Cell | | | | Hexagonal Cell | | | |
|--------|----------|-------------|------------|--------------|------------|----------------|------------|--------------|------------|
| | | Fiber (MPa) | | Matrix (MPa) | | Fiber (MPa) | | Matrix (MPa) | |
| | | σ_1 | σ_2 | σ_1 | σ_2 | σ_1 | σ_2 | σ_1 | σ_2 |
| A | 0 | 1.78 | -36.9 | 39.4 | -20.7 | 3.29 | -33.8 | 41.3 | -10.1 |
| | 0 | 54.3 | -104 | 63.4 | -35.5 | 51.2 | -91.0 | 63.4 | -21.8 |
| B | 90 | 59.0 | -217 | 65.4 | -36.3 | 55.2 | -204 | 66.6 | -22.9 |
| | 0 | 50.8 | -155 | 69.2 | -34.2 | 47.7 | -147 | 68.4 | -21.4 |
| C | 45 | 45.3 | -33.5 | 61.3 | -33.4 | 43.3 | -23.4 | 61.3 | -19.7 |
| | 90 | 55.9 | -291 | 71.4 | -35.4 | 52.2 | -283 | 71.1 | -22.7 |

Table 2-10. Percentage difference of principal stresses estimated by square and hexagonal unit cells. The negative sign indicates that micro-stress result estimated by the hexagonal unit cell is lower.

| Sample | θ | Fiber (MPa) | | Matrix (MPa) | |
|--------|----------|----------------|----------------|----------------|----------------|
| | | σ_1 (%) | σ_2 (%) | σ_1 (%) | σ_2 (%) |
| A | 0 | 84.7 | -8.56 | 4.76 | -51.2 |
| | 0 | -5.60 | -12.1 | -0.10 | -38.5 |
| B | 90 | -6.33 | -5.99 | 1.87 | -37.0 |
| | 0 | -6.16 | -4.92 | -1.19 | -37.5 |
| C | 45 | -4.57 | -30.1 | 0.03 | -41.2 |
| | 90 | -6.61 | -2.85 | -0.39 | -36.1 |

The laminate stresses are estimated by stress-strain relation for various laminate samples with principal material directions (L and T) in Table 2-8. The micro-stresses in fiber and matrix phases are estimated using the micromechanics methods and the principal stresses σ_1 and σ_2 are calculated based on the micro-stress results in Table 2-9. The difference in principal stresses estimated using the square and hexagonal cells are shown in Table 2-10.

For the unidirectional laminate (Sample A), the laminate stresses is zero under free boundary condition since the laminate undergoes free thermal contraction at cryogenic temperature in Table 2-8. However, the stresses at micro-scale are generated because of contraction between fiber and matrix. The micro-stresses in the fiber are very small compared to the matrix stresses. Therefore, the difference of maximum principal stresses in the fiber phase shows large in Table 2-10.

The maximum principal stress is relatively consistent for both square and hexagonal unit cells, but the hexagonal unit cell estimated that the minimum principal stress in the matrix is reduced by approximately 40%. The results show the hexagonal unit cell underestimates the micro-stresses.

The results from the finite element simulation can be used to compute the normal and shear stresses at the fiber/matrix interface in the unit-cell. The normal and tangential stress components were calculated using the transformation matrix.

$$\begin{bmatrix} \sigma_n \\ \sigma_s \\ \tau_{ns} \end{bmatrix} = \begin{bmatrix} \cos^2 \theta & \sin^2 \theta & 2 \sin \theta \cos \theta \\ \sin^2 \theta & \cos^2 \theta & -2 \sin \theta \cos \theta \\ -\sin \theta \cos \theta & \sin \theta \cos \theta & \cos^2 \theta - \sin^2 \theta \end{bmatrix} \begin{bmatrix} \sigma_x \\ \sigma_y \\ \tau_{xy} \end{bmatrix} \quad (2.6)$$

where θ is the angle measured from the x axis as shown in Figure 2-9.

The normal and shear stresses around the periphery of the fiber are investigated when the uniaxial laminate is subjected to the cryogenic temperatures $\Delta T = -405$ K without external loads. To compare the results for both unit cells, the interfacial stresses are plotted for $90^\circ < \theta < 270^\circ$. From the results shown in Figure 2-10 and 2-11 one can note that the absolute values of interfacial normal and shear stresses are lower for the hexagonal unit cell.

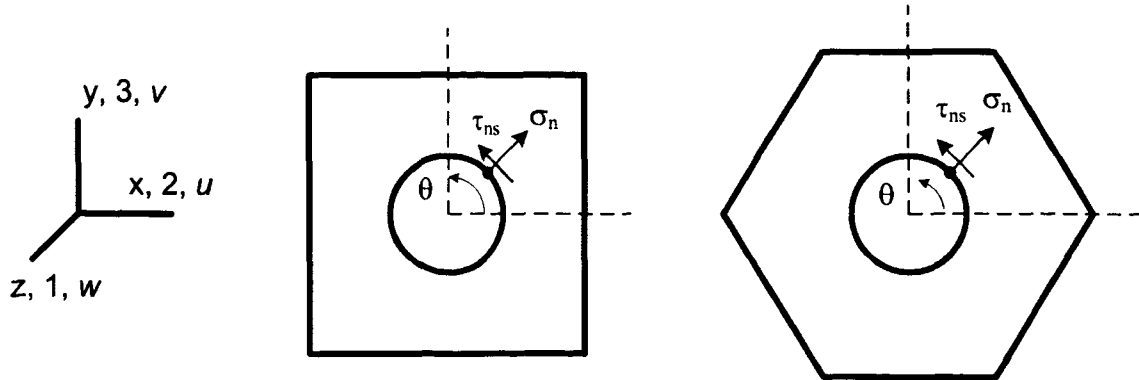


Figure 2-9. Normal and shear stresses at the fiber-matrix interface in square and hexagonal unit cells.

It explains that the interfacial fracture between fiber and matrix is less likely to occur in a hexagonal unit cell than in a square unit cell. In real composite, fiber distribution are in hexagonal patterns, the interfacial stresses can be reduced.

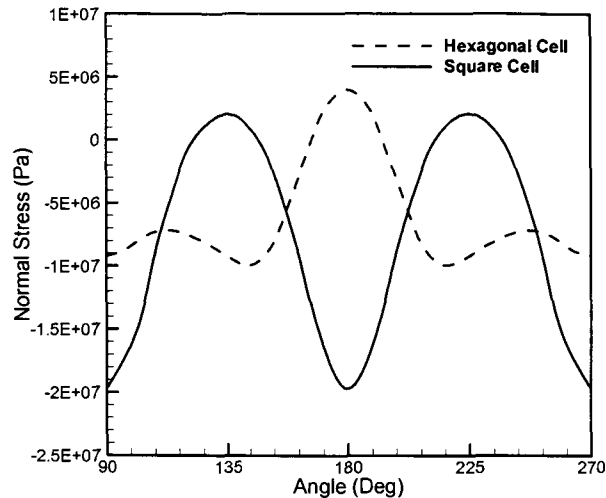


Figure 2-10. Interfacial normal stresses in uniaxial graphite/epoxy laminate system at $\Delta T = -405$ K.

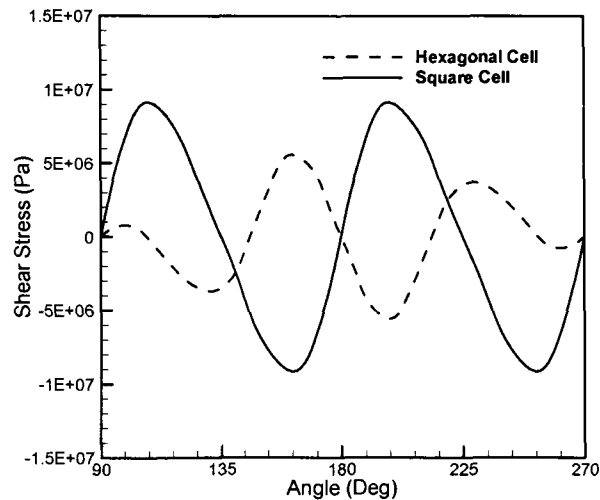


Figure 2-11. Interfacial shear stresses in uniaxial graphite/epoxy laminate system at $\Delta T = -405$ K.

Application to the Liquid Hydrogen Composite Tank

The micromechanics method is used to predict the failure of the liquid hydrogen composite tank due to combined thermal and external loads. The liquid hydrogen composite tank is made of a honeycomb composite sandwich structure [1]. The inner face sheet is a 13-ply, IM7/977-2 laminate (0.066 inch thick) with the stacking sequence $[45/90_3/-45/0_3/-45/90_3/45]_T$. The outer face sheet is a 7-ply, IM7/977-2 laminate (0.034 inch thick) with the stacking sequence $[65/0/-65/90/-65/0/65]_T$. The material properties

used for the IM7/977-2 laminates are estimated in Table 2-2. The honeycomb core is Korex 3/16-3.0 (1.5 inch thick). The elastic constants of the core are: $E_1 = E_2 = 4.14 \text{ MPa}$, $E_3 = 137.9 \text{ MPa}$, $G_{12} = 4.14 \text{ MPa}$, $G_{13} = 74.5 \text{ MPa}$, $G_{23} = 15.9 \text{ MPa}$, $\nu_{12} = 0.25$, $\nu_{13} = \nu_{23} = 0.02$. The thermal expansion of the honeycomb core is assumed to be zero.

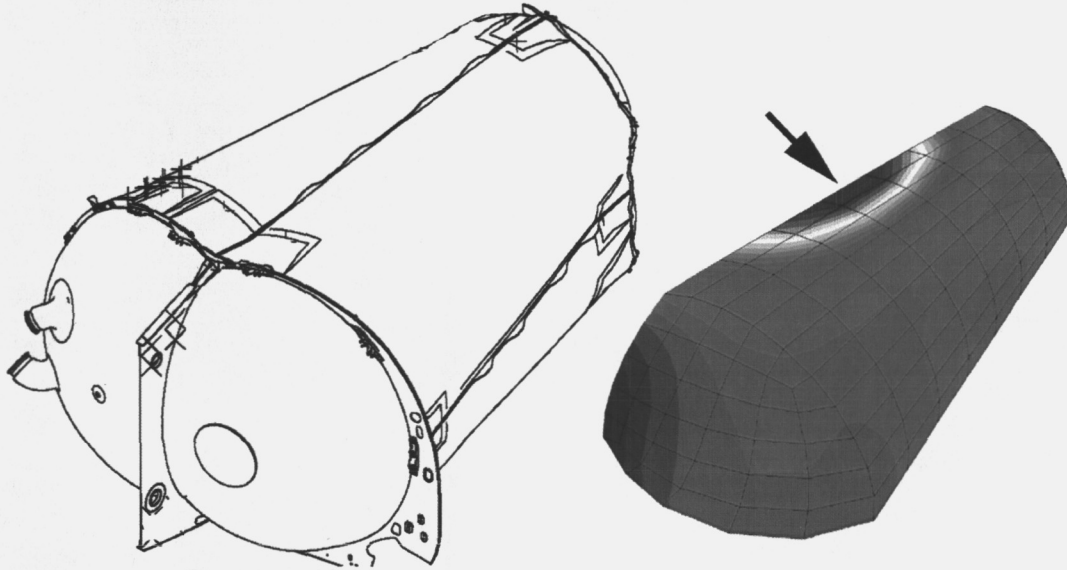


Figure 2-12. Maximum principal stress distribution in the LH2 Graphite/Epoxy composite tank. Tank pressure = 10 KPa and temperature = 50 K ($\Delta T = -405$ K).

The liquid hydrogen composite tank is subjected to appropriate boundary conditions in the ABAQUS[®] FE model to simulate the situation at which it failed during proof test [1]. The actual liquid hydrogen composite tank was modeled using 8-node solid elements (see Figure 2-12). The quarter model of the composite tank has 137 elements with 75 integration points in the thickness direction. The lay-up configuration of the composite laminates is specified in the layered solid elements. The IM7/997-2 laminate properties used for the macro-model are given in Table 2-5.

The macro-level analysis was performed for two cases. In the first case, the tank was exposed to cryogenic temperature without internal pressure. In the second case, an internal pressure was applied in addition to cryogenic temperature. The displacement contours shown in Figure 2-12 correspond to a pressure of 10 kPa and $\Delta T = -405$ K. The location denoted by the arrow in Figure 2-12 was selected for further investigation of failure due to micro-stresses. The macro-level strains and curvatures in longitudinal and transverse fiber directions at $T = 50 \text{ K}$ were computed using the finite element analysis (Tables 2-11 and 2-12). The micro-stresses in the inner and outer face sheets were calculated using the superposition method described in the previous section.

Table 2-11. Laminate macro-strains used to obtain the micro-stresses in the inner and outer face-sheets of the sandwich composite without internal pressure.

| Layer | θ | $\epsilon_L (10^{-3})$ | $\epsilon_T (10^{-3})$ | $\epsilon_Z (10^{-3})$ | $\gamma_{LT} (10^{-3})$ | $\gamma_{LZ} (10^{-3})$ | $\gamma_{TZ} (10^{-3})$ |
|--------------------|----------|------------------------|------------------------|------------------------|-------------------------|-------------------------|-------------------------|
| Inter Facesheet | 45 | -0.149 | -0.227 | -5.43 | -0.299 | 0.512 | -0.0831 |
| | 90 | -0.0386 | -0.338 | -5.43 | 0.0773 | 0.422 | 0.302 |
| | -45 | -0.226 | -0.150 | -5.43 | 0.299 | -0.0898 | -0.510 |
| | 0 | -0.338 | -0.0380 | -5.43 | -0.0748 | 0.296 | -0.425 |
| | -45 | -0.224 | -0.151 | -5.43 | 0.300 | -0.0965 | -0.508 |
| | 90 | -0.0374 | -0.337 | -5.43 | 0.0723 | 0.428 | 0.289 |
| | 45 | -0.152 | -0.222 | -5.43 | -0.300 | 0.506 | -0.103 |
| Core | — | -0.337 | -0.0367 | -5.43 | -0.0697 | 0.283 | -0.431 |
| Outer Facesheet | 65 | -0.0899 | -0.203 | -5.51 | -0.298 | 0.543 | -0.452 |
| | 0 | -0.296 | 0.00423 | -5.51 | 0.106 | -0.182 | -0.684 |
| | -65 | -0.00858 | -0.283 | -5.51 | 0.162 | -0.698 | -0.123 |
| | 90 | 0.00447 | -0.296 | -5.51 | -0.107 | 0.686 | -0.185 |
| | -65 | -0.00792 | -0.283 | -5.51 | 0.161 | -0.701 | -0.121 |
| | 0 | -0.296 | 0.00470 | -5.51 | 0.108 | -0.188 | -0.687 |
| | 65 | -0.0904 | -0.0200 | -5.51 | -0.300 | 0.544 | -0.463 |

Table 2-12. Laminate macro-strains used to obtain the micro-stresses in the inner and outer face-sheets of the sandwich composite subjected to a pressure of 10 KPa.

| Layer | θ | $\epsilon_L (10^{-3})$ | $\epsilon_T (10^{-3})$ | $\epsilon_Z (10^{-3})$ | $\gamma_{LT} (10^{-3})$ | $\gamma_{LZ} (10^{-3})$ | $\gamma_{TZ} (10^{-3})$ |
|--------------------|----------|------------------------|------------------------|------------------------|-------------------------|-------------------------|-------------------------|
| Inter Facesheet | 45 | -0.147 | 0.419 | -5.90 | -0.731 | 3.11 | -3.69 |
| | 90 | 0.501 | -0.230 | -5.90 | -0.563 | 4.81 | -0.407 |
| | -45 | 0.412 | -0.144 | -5.90 | 0.732 | -3.67 | -3.13 |
| | 0 | -0.233 | 0.500 | -5.90 | 0.553 | -0.371 | -4.81 |
| | -45 | 0.405 | -0.141 | -5.89 | 0.734 | -3.64 | -3.16 |
| | 90 | 0.498 | -0.236 | -5.89 | -0.543 | 4.81 | -0.335 |
| | 45 | -0.138 | 0.398 | -5.89 | -0.735 | 3.18 | -3.62 |
| Core | — | -0.238 | 0.497 | -5.89 | 0.534 | -0.299 | -4.81 |
| Outer Facesheet | 65 | 0.303 | -0.366 | -5.57 | -0.622 | 5.30 | 0.118 |
| | 0 | -0.485 | 0.422 | -5.57 | -0.115 | 2.36 | -4.75 |
| | -65 | 0.214 | -0.280 | -5.57 | 0.770 | -3.31 | -4.15 |
| | 90 | 0.421 | -0.487 | -5.56 | 0.119 | 4.75 | 2.37 |
| | -65 | 0.212 | -0.280 | -5.56 | 0.774 | -3.30 | -4.17 |
| | 0 | -0.489 | 0.421 | -5.56 | -0.122 | 2.39 | -4.75 |
| | 65 | 0.306 | -0.375 | -5.56 | -0.618 | 5.32 | 0.165 |

Table 2-13. Maximum and minimum principal stresses in the fiber and matrix phases in the inner and outer face-sheets of the sandwich composite without internal pressure.

| Layer | θ | Without tank pressure at $T = 50K$ | | | |
|-----------------|----------|------------------------------------|------------|--------------|------------|
| | | Fiber (MPa) | | Matrix (MPa) | |
| | | σ_1 | σ_2 | σ_1 | σ_2 |
| Inter Facesheet | 45 | 58.8 | -138 | 70.9 | -2.71 |
| | 90 | 57.8 | -107 | 69.3 | -2.47 |
| | -45 | 59.6 | -157 | 71.0 | -2.49 |
| | 0 | 60.6 | -185 | 71.3 | -2.73 |
| | -45 | 59.6 | -156 | 71.0 | -2.50 |
| | 90 | 57.8 | -107 | 69.3 | -2.50 |
| | 45 | 58.8 | -139 | 70.9 | -2.74 |
| Core | — | — | — | — | — |
| | 65 | 59.1 | -123 | 71.3 | -3.79 |
| | 0 | 61.1 | -175 | 71.7 | -3.74 |
| | -65 | 58.2 | -101 | 70.4 | -3.99 |
| Outer Facesheet | 90 | 58.1 | -97.5 | 70.3 | -3.87 |
| | -65 | 58.2 | -101 | 70.4 | -4.00 |
| | 0 | 61.1 | -175 | 71.7 | -3.75 |
| | 65 | 59.1 | -123 | 71.4 | -3.82 |

Table 2-14. Maximum and minimum principal stresses in the fiber and matrix phases in the inner and outer face-sheets of the sandwich composite subjected to a pressure of 10 KPa.

| Layer | θ | Tank pressure = 10KPa at $T = 50K$ | | | |
|-----------------|----------|------------------------------------|------------|--------------|------------|
| | | Fiber (MPa) | | Matrix (MPa) | |
| | | σ_1 | σ_2 | σ_1 | σ_2 |
| Inter Facesheet | 45 | 77.8 | -167 | 101 | -21.2 |
| | 90 | 121 | -33.5 | 93.2 | -27.2 |
| | -45 | 92.5 | -37.1 | 96.4 | -23.0 |
| | 0 | 79.0 | -162 | 90.0 | -14.1 |
| | -45 | 90.8 | -38.1 | 96.4 | -22.8 |
| | 90 | 121 | -33.7 | 92.9 | -27.1 |
| | 45 | 77.5 | -166 | 101 | -21.4 |
| Core | — | — | — | — | — |
| | 65 | 84.8 | -78.0 | 93.1 | -27.5 |
| | 0 | 80.8 | -242 | 99.3 | -16.2 |
| | -65 | 74.7 | -76.8 | 96.9 | -19.0 |
| Outer Facesheet | 90 | 100 | -45.7 | 96.2 | -25.2 |
| | -65 | 74.7 | -77.3 | 97.0 | -19.0 |
| | 0 | 80.8 | -244 | 99.5 | -16.3 |
| | 65 | 85.5 | -77.7 | 93.0 | -27.6 |

The results of the maximum principal stresses in the fiber and matrix phases in each layer of the laminate are shown in Tables 2-13 and 2.14. When the cryogenic temperature is applied to the composite tank without tank pressure, the maximum principal stress in the matrix phase (70 MPa) is below its strength (100MPa). The result indicates micro-stress in the matrix phases, although very high, is not enough to initiate microcracks. However, when the tank pressure increases and reaches 10KPa, micro-stress in the matrix in the inner facesheet exceeds the tensile strength indicating the possibility of micro-crack development.

CHAPTER 3

FRACTURE TOUGHNESS FOR A TRANSVERSE CRACK IN LAMINATED COMPOSITES AT CRYOGENIC TEMPERATURES

Stress singularity for the crack tip normal to the ply-interface is used to determine the conditions under which delaminations will initiate in a laminated composite. Stress singularity at a crack tip normal to the interface in fiber-reinforced composites with different stacking sequences is investigated using analytical and finite element approaches. The stress singularity is used to predict the stress distribution in the vicinity of the crack tip. The fracture loads for several different laminate systems are determined using the four-point bending experiments. The fracture toughness is determined using the finite element analysis when the laminated specimen model is subjected to the fracture load obtained in the test.

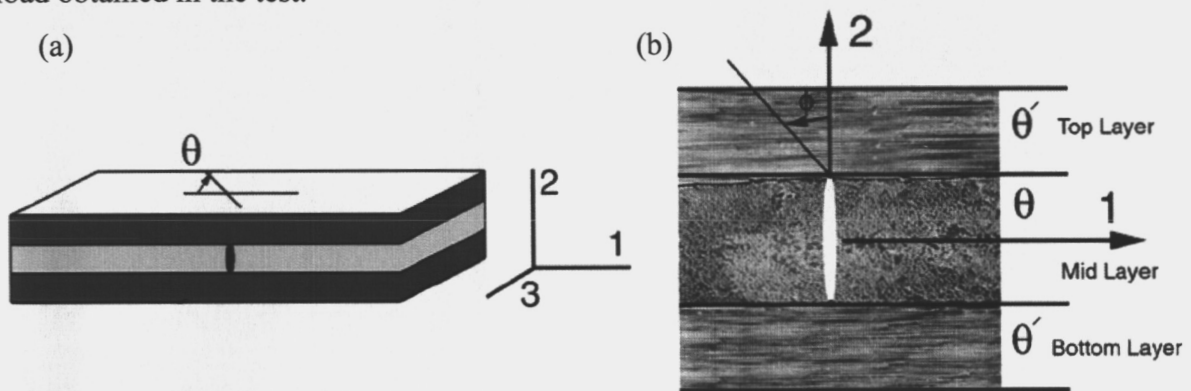


Figure 3-1. (a) Geometry of interfacial fracture specimens, (b) A crack normal to laminate interface with different stacking sequence.

Stress Singularities at a Crack-tip Normal to a Ply-interface

Stress singularity for a transverse crack in a composite laminate is determined using an analytical method. The analytical methods to determine the singularity for a transverse crack in a laminated composite (bi-material interface) can be found in Ting's analysis [14-15]. The details of the Ting's methods are described in Appendix A. In this approach the general solutions of displacement and stresses are derived using strain-displacement, stress-strain and equilibrium equations in terms of arbitrary constants and singularities. The singularities are determined when the boundary conditions on the crack surfaces and continuity conditions at the interface are satisfied.

The analytic approach is performed to estimate the singularity of a transverse crack of glass/epoxy and graphite/epoxy (IM7/977-2) composites with stacking sequence $[0_3]_T$, $[0/90/0]_T$ and $[90/0/90]_T$ in Figure 3-1. The crack tip of the transverse crack is placed at the interface between top and mid layers. The laminate properties of graphite/epoxy and glass/epoxy are shown in Table 3-1 [26]. The singularity results are compared with the finite element results. The commercial computer program MATLAB[®] is used to solve the analytical equations.

Table 3-1. Material properties of glass/epoxy and carbon/epoxy laminates.

| | E-glass/epoxy | Graphite/epoxy |
|---|---------------|----------------|
| E_{11} (GPa) | 38.6 | 160.9 |
| E_{22}, E_{33} (GPa) | 8.27 | 9.62 |
| G_{12}, G_{13} (GPa) | 4.14 | 6.32 |
| G_{23} (GPa) | 3.18 | 4.22 |
| ν_{12}, ν_{13} | 0.25 | 0.32 |
| ν_{23} | 0.3 | 0.14 |
| α_{11} ($10^{-6}/^{\circ}\text{C}$) | 8.60 | -0.512 |
| α_{22}, α_{33} ($10^{-6}/^{\circ}\text{C}$) | 22.1 | 16.3 |

Finite element analysis is used not so much to verify the results from the analytical model but to determine the mesh refinement needed to obtain the proper singularity at the crack tip. In the finite element analysis a laminated composite beam was modeled using 8-node solid elements with 20 integration points as shown in Figure 3-2. Glass/epoxy and graphite/epoxy (IM7/977-2) composites with stacking sequence $[0_3]_T$, $[0/90/0]_T$ and $[90/0/90]_T$ are chosen to verify the stress singularity of the transverse crack. The ply thickness was taken as 2.2 mm. The length of the beam was 146 mm and the width 18.7 mm. An initial crack normal to a ply-interface is placed at the center of the beam subjected to tensile or bending loads (see Figure 3-3). The crack tip is located at the interface of the top and mid layers. The region surrounding the crack-tip was refined using 31,000 quadratic solid elements. The commercial finite element software ABAQUS[®] was used for this purpose.

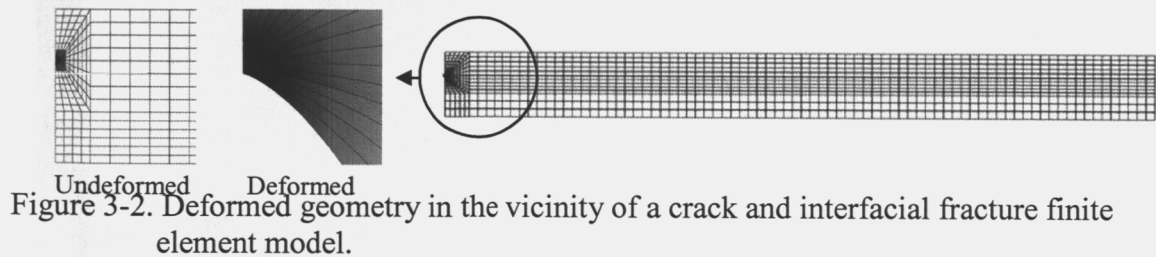
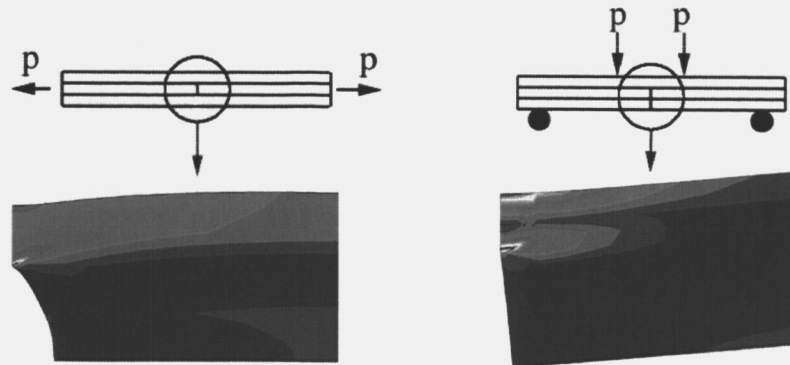


Figure 3-2. Deformed geometry in the vicinity of a crack and interfacial fracture finite element model.

Figure 3-3. Contour plots of stress distribution for a $[0/90/0]_T$ composite model at a crack-tip under tensile and bending loads.

The composite beam model is subjected to four-point bending and/or tensile loading conditions as shown in Figure 3-3. For the tensile case, uniform displacement in the x -direction is applied at the end of the beam. For bending cases, the beam is simply supported at 63.7 mm away from the crack. The top load is located at 19.5 mm away from the crack. The normal stresses ahead of the transverse crack-tip for tensile and bending cases are shown in Figure 3-4.

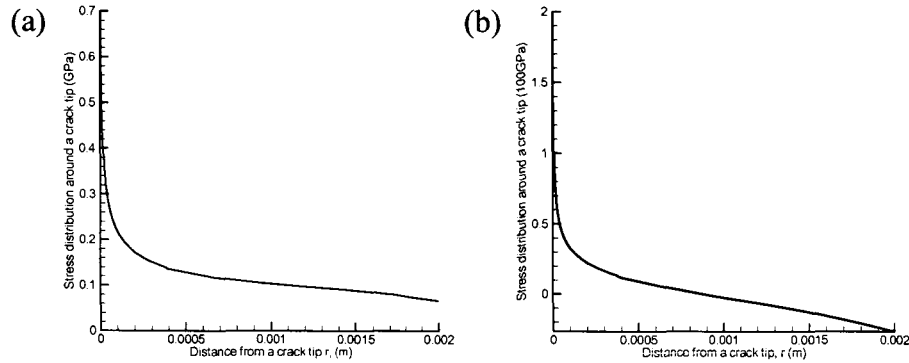


Figure 3-4. Stress distribution under (a) tensile loads; (b) bending loads.

A logarithmic plot of the normal stresses as a function of distance from the crack tip is used to determine the singularity in the FE model. The crack tip stress field is assumed to be of the form $\sigma = K_I r^{-\lambda}$, where $-1 < \lambda < 0$. The stress singularity λ is estimated by calculating the slope of the logarithmic plot of normal stress as a function of distance r ahead of the crack-tip.

Table 3-2. Singularity results of E-glass/epoxy.

| E-glass/epoxy | | | | | |
|--------------------|------------------------|-------------------------|-----------|---------|-----------|
| Layers | Analytical (Ting's) | FEM (ABAQUS) Tensile | Error (%) | Bending | Error (%) |
| [0 ₃] | 0.50 | 0.50 | 0.3 | 0.50 | 0.2 |
| [0/90/0] | 0.38 | 0.38 | 1.1 | 0.39 | 2.3 |
| [90 ₃] | 0.50 | 0.50 | 0.3 | 0.50 | 0.1 |
| [90/0/90] | 0.63 | 0.63 | 1.1 | 0.61 | 3.1 |

Table 3-3. Singularity results of graphite/epoxy.

| Graphite/epoxy | | | | | |
|--------------------|------------------------|-------------------------|-----------|---------|-----------|
| Layers | Analytical (Ting's) | FEM (ABAQUS) Tensile | Error (%) | Bending | Error (%) |
| [0 ₃] | 0.50 | 0.50 | 0.5 | 0.50 | 0.0 |
| [0/90/0] | 0.26 | 0.27 | 2.6 | 0.29 | 7.8 |
| [90 ₃] | 0.50 | 0.50 | 0.5 | 0.50 | 0.1 |
| [90/0/90] | 0.71 | 0.70 | 4.8 | 0.69 | 5.9 |

The stress singularities determined from the finite element analyses are compared with the analytical results for various laminates in Tables 3-2 and 3-3. There seems to be a good agreement between the two sets of results. The maximum difference between the two values is insignificant. When the laminate orientation of the materials on both side of

ply-interface are identical as in the case of unidirectional laminates, $([0_3]$ and $[90_3])$, the singularity $\lambda = 0.5$. The 0° layer is stiffer than the 90° layer in the plane direction since the load carried by the laminates is shared with the fiber and the matrix. When the laminate ahead of the crack tip is stiffer, as in $[0/90/0]$ laminates, the stress singularity λ becomes less than 0.5. It is greater than 0.5 when the crack is in the 0° layer is touching the $0/90$ interface as in $[90/0/90]$ laminates. The results provide confidence in the accuracy of the finite element models in capturing the singularity for transverse cracks in a composite laminate. Then the FE model can be used to analyze several composite systems used in fracture tests.

Fracture Toughness at Room Temperature

Four-point bending experiments are performed to determine the fracture loads of laminated beam specimens at room temperature as shown in Figure 3-5. The four-point bending test has the advantages that it would yield more accurate and repeatable results as the transverse crack is in a region under constant bending moment without any transverse shear force. Even a small offset of the loading point with respect to the crack location will not significantly affect the results.

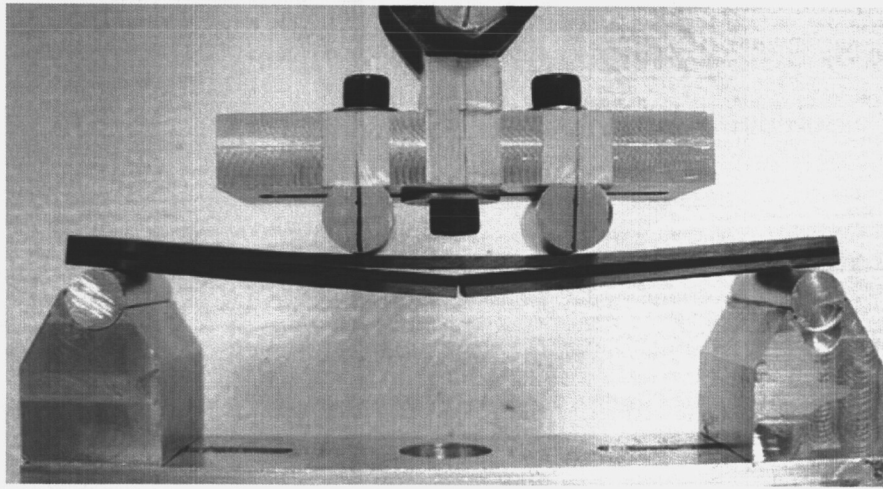


Figure 3-5. Four-point bending test to determine the fracture load.

The proposed specimen has three layers of graphite/epoxy laminate with stacking sequence $[0/90/0]_T$. The top and bottom layers for all specimens have same thickness of 2.4 mm and the mid-layer has various thicknesses, 1.8, 2.4 and 3.0 mm. The dimensions of specimens are listed in Table 3-4. An initial crack was created at the center of the specimen below the top layer. The notch was cut using a fine diamond saw, and then the razor blade is used to sharpen the crack tip. The initial crack tip is located in the mid-layer and below the ply-interface of the top layer. The specimen is simply supported at 63.7 mm away from the crack. The top loads are applied at a distance of 19.5 mm from the crack. The bending tests were conducted under displacement control in a material testing machine at a loading rate of 1.0 mm/min.

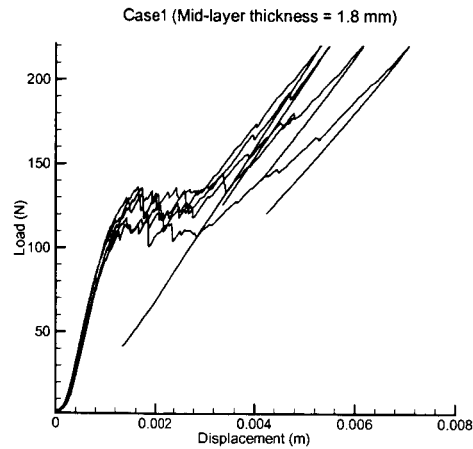


Figure 3-6. Load-displacement curves of four-point bending tests at room temperature for the Specimen 1.

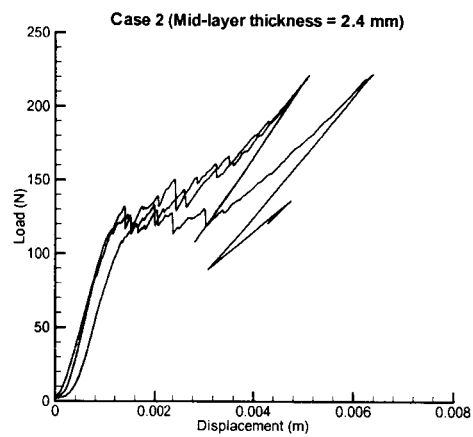


Figure 3-7. Load-displacement curves of four-point bending tests at room temperature for the Specimen 2

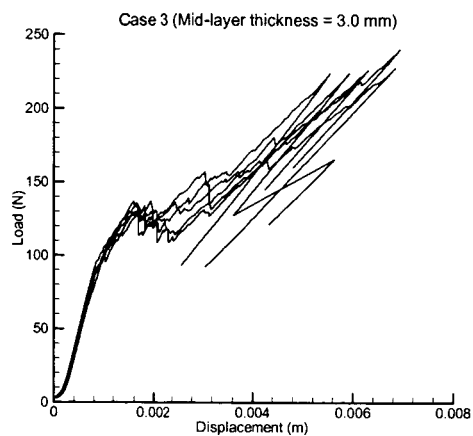


Figure 3-8. Load-displacement curves of four-point bending tests at room temperature for the Specimen 3

The load-deflection results of various specimens are shown in Figures 3-6-3-8. The load increases linearly until the crack-tip reaches the ply-interface of the top layer. When the crack reaches the interface, the load does not increase further since more strain energy is required to deflect the crack to the ply-interface. After the interfacial fracture initiates, and as the crack propagates as a delamination, the stiffness of the specimen reduces as indicated by the slope of the load-deflection curve. The fracture loads are measured immediately before interfacial fracture initiates. As results, the fracture load is linearly proportional to the thickness of the mid-layer in Table 3-5. The fracture loads for the three different specimens are listed in Table 3-6. One can note that the fracture load increases with the thickness of the middle 90° layer.

Table 3-4. Dimensions of specimens and various mid-ply thickness.

| [0/90/0] | Length (mm) | Width (mm) | Layer Thickness | |
|------------|-------------|------------|-------------------------------|---------------------|
| | | | Top and bottom layer, 0° (mm) | Mid layer, 90° (mm) |
| Specimen 1 | 145.4 | 18.6 | 2.4 | 1.8 |
| Specimen 2 | 146.2 | 18.7 | 2.4 | 2.4 |
| Specimen 3 | 145.7 | 18.8 | 2.4 | 3.0 |

Table 3-5. Fracture load and fracture toughness at room and cryogenic temperatures.

| [0/90/0] | Room Temperature ($T = 300$ K) | | Cryogenic Temperature ($T = 77$ K) | |
|------------|---------------------------------|-----------------------------------|-------------------------------------|-----------------------------------|
| | F_f (N) | K_{IC} (MPa-m ^{0.29}) | F_f (N) | K_{IC} (MPa-m ^{0.29}) |
| Specimen 1 | 122 | 58.1 | 88.1 | 55.6 |
| Specimen 2 | 127 | 57.9 | 81.5 | 58.1 |
| Specimen 3 | 133 | 58.0 | 74.7 | 58.8 |

Finite element analyses of the test specimens were performed to determine the detailed stress field in the vicinity of the crack tip corresponding to the fracture loads. Due to symmetry one-half of the specimen is modeled. The laminate properties of graphite/epoxy given in Table 3-1 are used for the FE model. A contour plot of the stress distribution is shown in Figure 3-9.

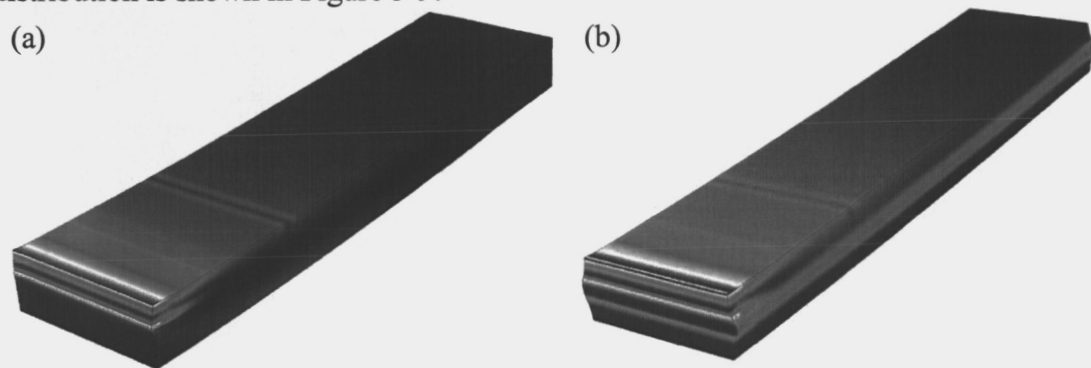


Figure 3-9. Stress distribution for the 4-Pt bending simulation at (a) room temperature; (b) cryogenic temperature.

The fracture toughness can be calculated in two ways. The first method is similar to the “stress matching” [29] as described by the equation below (see Figure 3-10):

$$K_I = \lim_{r \rightarrow 0} \sigma(r)r^\lambda \quad (3.1)$$

In the second method a logarithmic plot of σ vs. r is used to determine the best value of K by fitting (see Figure 3-11)

$$\sigma(r) = K_I r^{-\lambda} \quad (3.2)$$

In both methods the singularity λ derived from the analytical method was used.

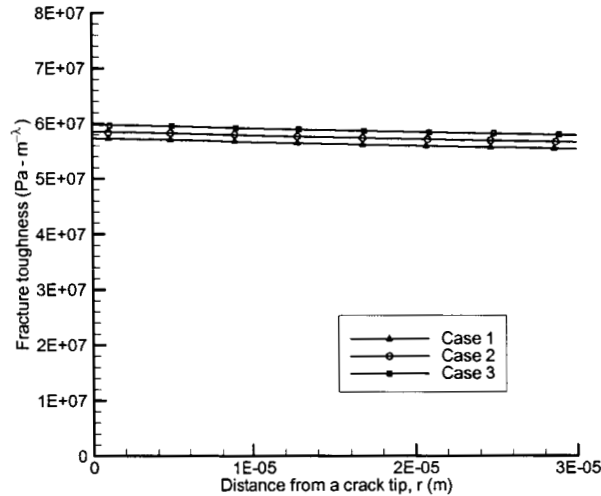


Figure 3-10. Variation of $\bar{K} = \sigma r^\lambda$ with the distance from the crack tip at room temperature.

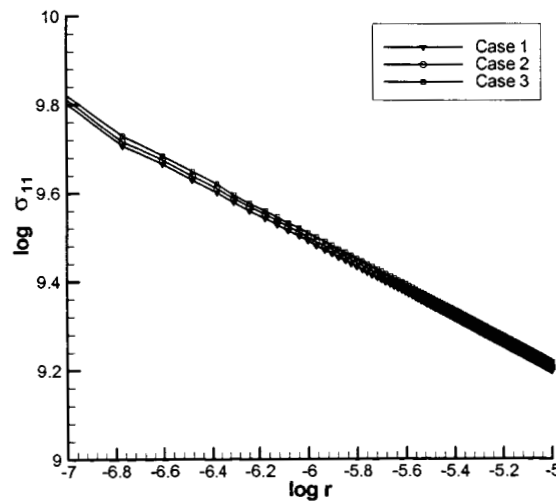


Figure 3-11. Logarithmic plot of the stresses as a function of distance from the crack-tip.

From the results shown in Table 3-5, one can note that the increase in fracture load is about 8% with 67% increase of mid-ply thickness. However the variation in the fracture toughness is about less than ½%. The results shows fracture toughness is independent to

the mid-ply thickness. Fracture toughness is only dependent to local properties near a crack tip, but not global properties of the laminate system.

Fracture Toughness at Cryogenic Temperatures

The effect of cryogenic temperature on fracture toughness is investigated by performing the fracture tests in liquid Nitrogen temperature. Liquid nitrogen (LN2) is used as the cryogenic refrigerant for several reasons. It is chemically inactive and non-toxic. Liquid nitrogen is a colorless fluid like water. The boiling temperature of LN2 is 77 K.

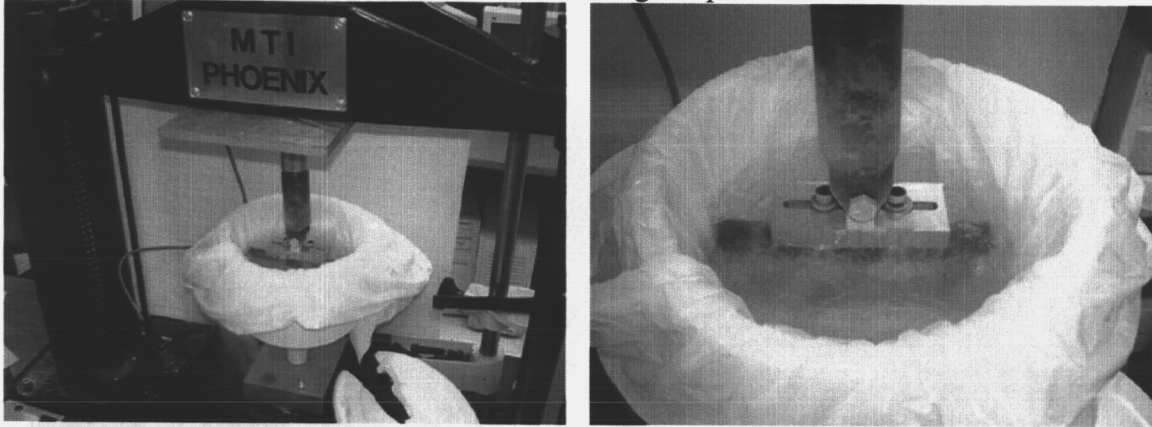


Figure 3-12. Cryogenic experimental setup of the four-point bending test.

The beam specimens are submerged initially in LN2 for about 5 minutes to reduce thermal gradients in the specimens as shown in Figure 3-12. The specimen is placed in the cryogenic container with the liquid nitrogen. When temperature of specimen reaches the LN2 boiling temperature, LN2 boiling disappears. During this process, some specimens experience delamination on the edge of mid-ply as shown in Figure 3-13.

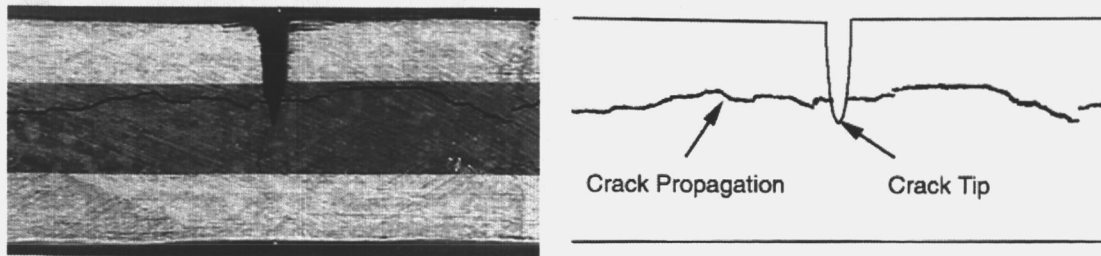


Figure 3-13. Crack propagation in the 90° layer of a graphite/epoxy laminate at cryogenic temperature.

Finite element analysis is performed to investigate the formation of edge delamination in the laminated specimen. The quarter region of an actual specimen is modeled using 8-node 3-D solid elements. A contour plot of stresses in 2-direction is shown in Figure 3-14 when the FE model is subjected to cryogenic temperature ($T = 77$ K).

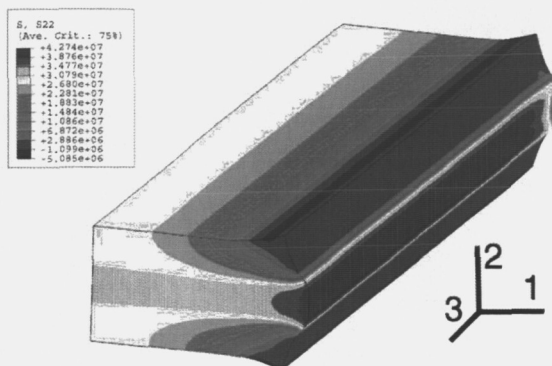


Figure 3-14. Contour plot of stresses normal to ply direction near the free-edge in a graphite/epoxy laminate at cryogenic temperature.

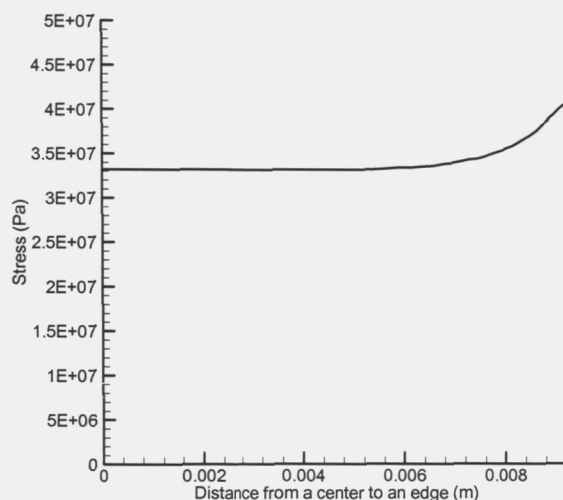


Figure 3-15. Load-displacement curves from four-point bending tests at cryogenic temperature. The mid-ply thickness and hence the specimen thickness varied from specimen to specimen.

The stresses in 2-direction stay constant in 80% of the width and increases sharply near the edge as shown in Figure 3-15. Since graphite/epoxy composite has negative longitudinal CTE in 3-direction (see Table 3-1), the mid-layer expands and the top and bottom layer shrinks at cryogenic temperature. Therefore, Mode I fracture behavior can be expected at the edge. The result predicts that crack length of the edge delamination is not too deep to affect the experiment results.

The four-point bending test fixture is placed in an insulated container and LN2 is filled up slowly. The LN2 boiling disappears when the temperature of the test fixture becomes stable. During experiment, LN2 is continuously added into the container so that specimen is completely submerged since LN2 vaporizes due to the heat loss to atmosphere. The four-point bending test is performed following the previous procedure for room temperature tests.

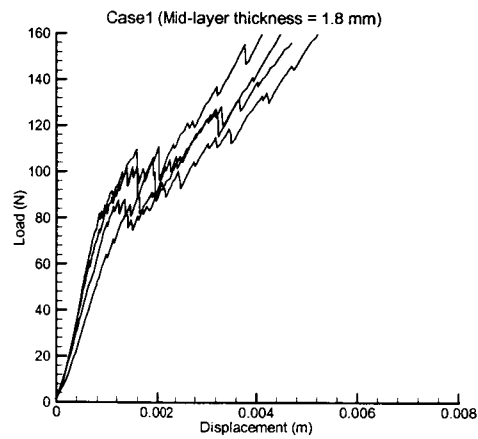


Figure 3-16. Load-displacement curves from four-point bending tests at cryogenic temperature for the Specimen 1

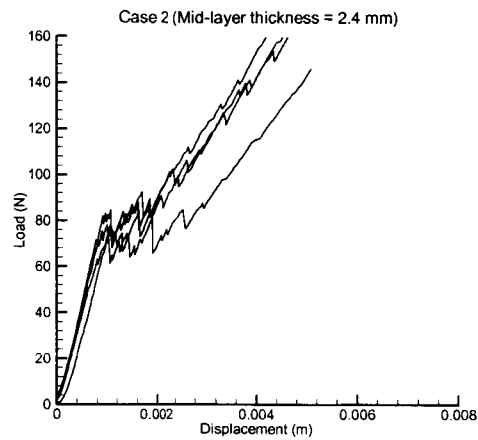


Figure 3-17. Load-displacement curves from four-point bending tests at cryogenic temperature for the Specimen 2

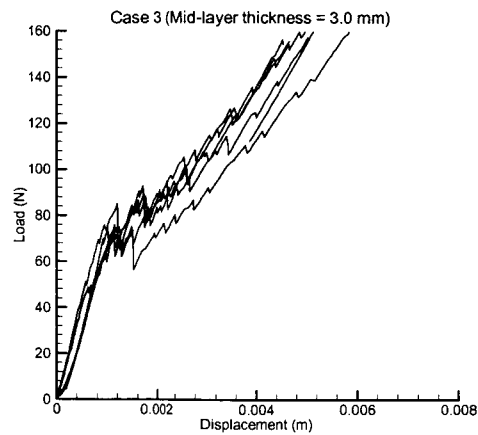


Figure 3-18. Load-displacement curves from four-point bending tests at cryogenic temperature for the Specimen 3.

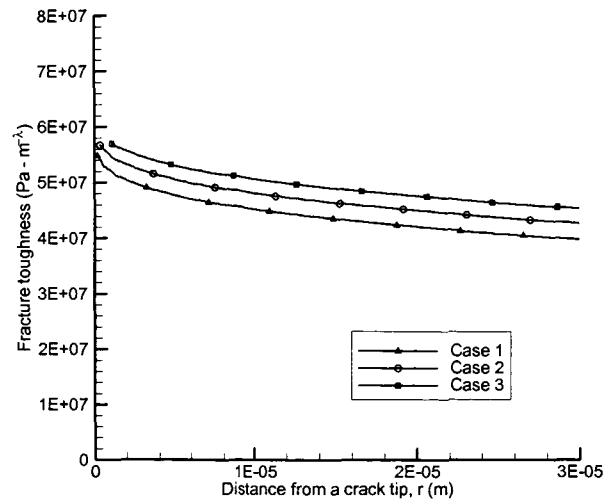


Figure 3-19. Variation of $\bar{K} = \sigma r^{1/2}$ with the distance from the crack tip at cryogenic temperature.

The load-displacement results are shown in Figures 3-16 through 3-18. Fracture load decreases 15% with 67% increase of the mid-ply thickness in Table 3-5. Fracture load decrease may be due to material degradation as micro-crack density increases at cryogenic temperature. Fracture toughness at cryogenic temperature is predicted using the finite element analysis. The contour plot of the stress distribution is shown in Figure 3-9. Fracture toughness is calculated following the same procedure as described in the previous section for room temperature tests. Variation of $\bar{K} = \sigma r^{1/2}$ with the distance from the crack tip is shown in Figure 3-19. Although the fracture loads decreases by 15% from Specimen 1 to Specimen 3, fracture toughness increases by only 5%. The variation of fracture toughness between the three specimens tested at cryogenic temperature is insignificant. The result indicates that fracture toughness is not significantly affected by the cryogenic conditions. But, the fracture load significantly decreases due to thermal stresses present in the vicinity of the crack tip. For both cases at room and cryogenic temperature, fracture toughness is estimated as 58 MPa. The result indicates fracture toughness is a characteristic property not governed by temperature changes.

It should be noted that the specimen dimensions and geometry are nominally the same for room temperature and cryogenic temperature tests are the same. But, the fracture load is significantly lower at cryogenic temperature. However the fracture toughness, the critical stress intensity factor, seems to be the same although we input lower loads in the finite element model. This is because there are significant thermal stresses at cryogenic temperature which increases the stress intensity factor to a higher value.

CHAPTER 4

PERMEABILITY TESTING OF COMPOSITE MATERIALS FOR A LIQUID HYDROGEN STORAGE SYSTEM

The permeability is defined by the amount of gas that passes through a given material of unit area and unit thickness under a unit pressure gradient in unit time. The SI unit of the permeability is mol/sec/m/Pa. Experiments were performed to investigate the effect of cryogenic cycling on permeability of laminated composites and to provide useful comparison of permeabilities of various composite material systems.

Standard Test Method for Determining Gas Permeability

The standard test method for determining gas permeability is documented in ASTM D1434-82 (Re-approved in 1997) "Standard Test Method for Determining Gas Permeability Characteristic of Plastic Film and Sheet [18]." The permeability can be measured by two methods, manometric determination method and volumetric determination methods. The permeability experiment using the monometric determination method is shown in Figure 4-1. The lower pressure chamber is initially vacuumed and the transmission of the gas through the test specimen is indicated by an increase in pressure.

The permeability is measured using volumetric determination as shown in Figure 4-2. The lower pressure chamber is exposed to atmospheric pressure and the transmission of the gas through the test specimen is indicated by a change in volume. The gas volume-flow rate is measured by recording the rise of liquid indicator in a capillary tube per unit time. The gas transmission rate (GTR) is calculated using the ideal gas law. The permeance is determined as the gas transmission rate per pressure differential across a specimen. The permeability is determined by multiplying permeance by the specimen thickness.

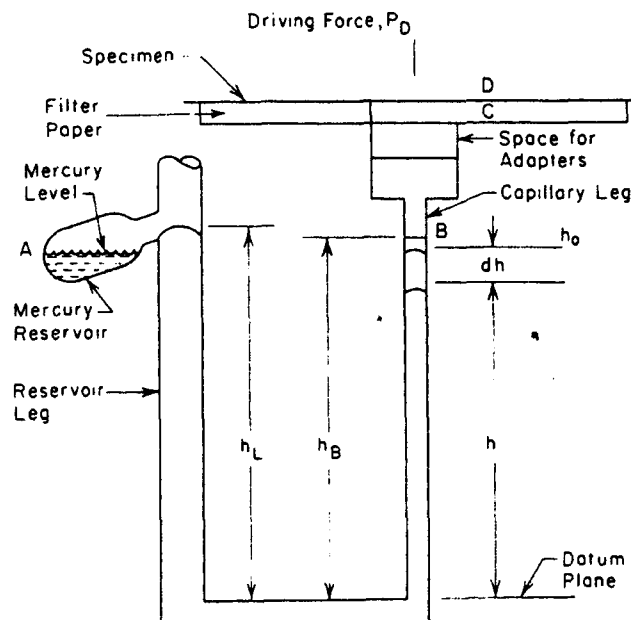


Figure 4-1. Permeability experimental setup for manometric determination method.

The monometric determination method was not considered for this study since it is dangerous to handle the mercury compound which is considered as a health hazardous material. Therefore, the permeability facility was constructed based on the volumetric determination method as shown in Figure 4-1.

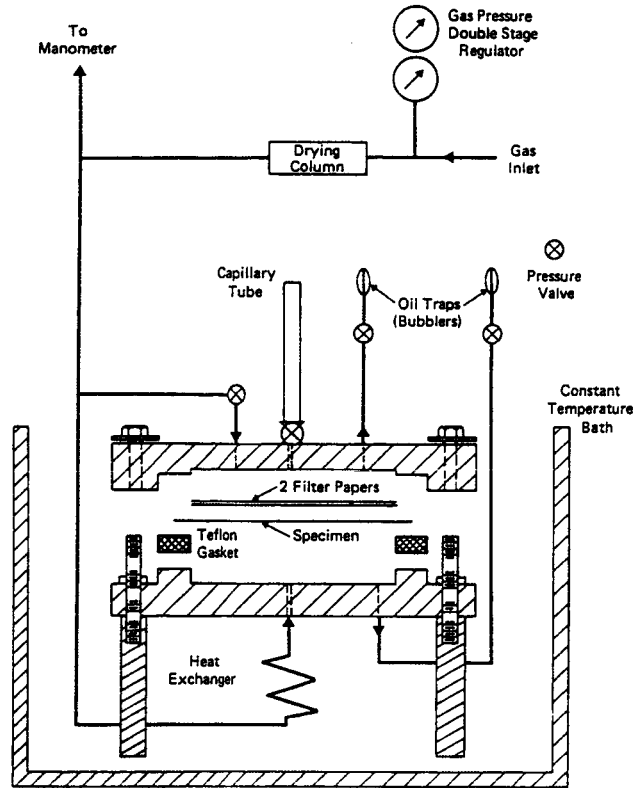


Figure 4-2. Permeability experimental setup for volumetric determination method.

Permeability Apparatus

This apparatus basically consists of a specimen placed between two chambers as shown in Figure 4-3. The test gas is pressurized in the upstream chamber. The gas permeates through one side of the specimen and escapes out of the other side. The escaped gas is collected in the downstream chamber and flows into a glass capillary tube. The amount of gas escaping per unit time is measured. The permeance is determined by gas transmitted rate and the partial pressure differential across the specimen. The permeability \bar{P} is defined by the product of permeance P and the specimen thickness t .

The gauge pressure of the gas in the upper upstream chamber is measured using a pressure transducer (P-303A from the Omega Engineering Inc). The ambient pressure is measured by a barometric sensor (2113A from the Pasco Scientific). A precision pressure regulator provides constant gas pressure to the upstream chamber. The ambient temperature was measured using a glass capillary thermometer.

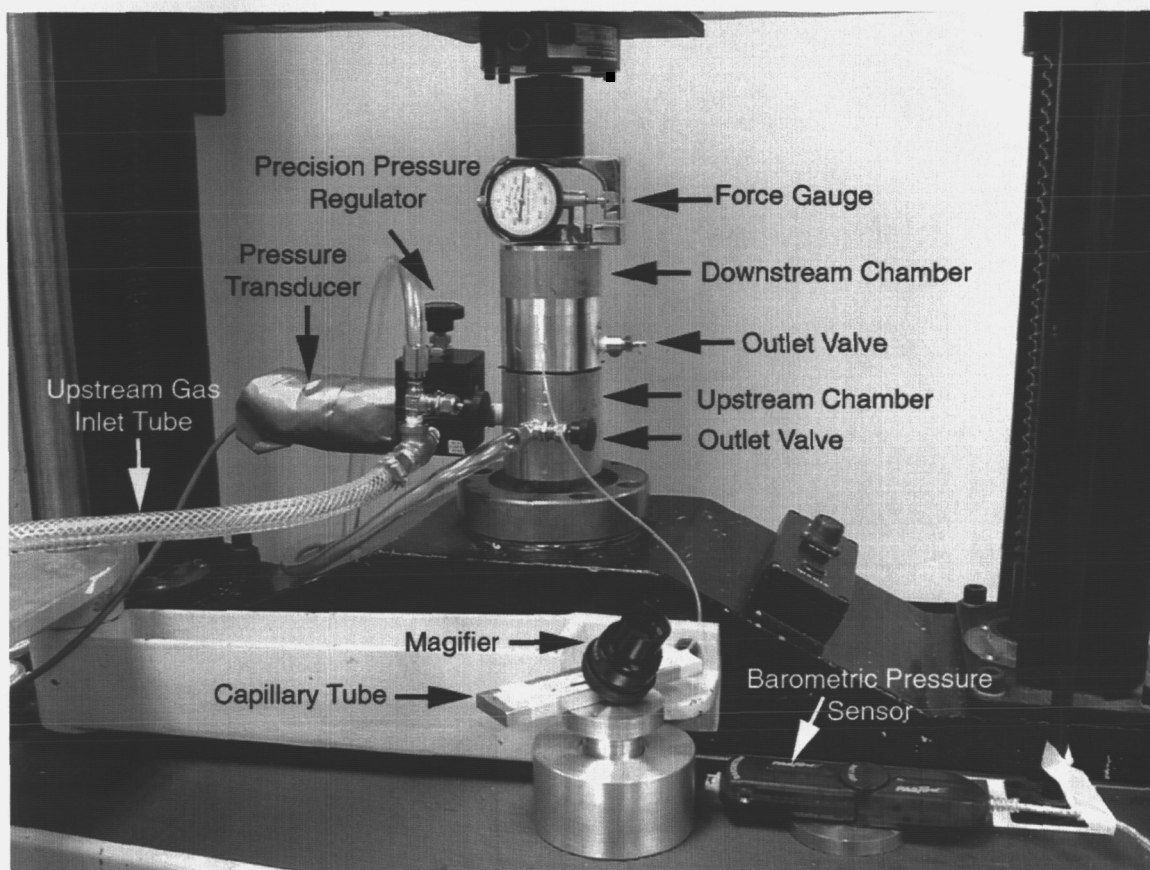


Figure 4-3. Permeability testing apparatus.

The specimens are mounted horizontally between the upstream and downstream chambers and clamped firmly by applying a compressive load as shown in Figure 4-4. The specimen is sealed with a rubber gasket and an O-Ring (38 mm inner diameter). A force gauge mounted at the top measures the compressive load to ensure that the same amount of compressive load is applied on the specimens for every test. The compressive load should be enough to prevent gas leakage, but should not damage the specimens. The upstream chamber has an inlet vent and an outlet vent. The inlet vent allows the gas flow into the upstream chamber and the outlet vents is used to purge the test gas to atmosphere (Figure 4-4). The downstream chamber has two outlet vents. One is used to purge the test gas to atmosphere and the other allows the gas flow to the glass capillary tube for measurements. The sensitivity of permeability measurement can be improved by increasing the gas transmitting area of a specimen.

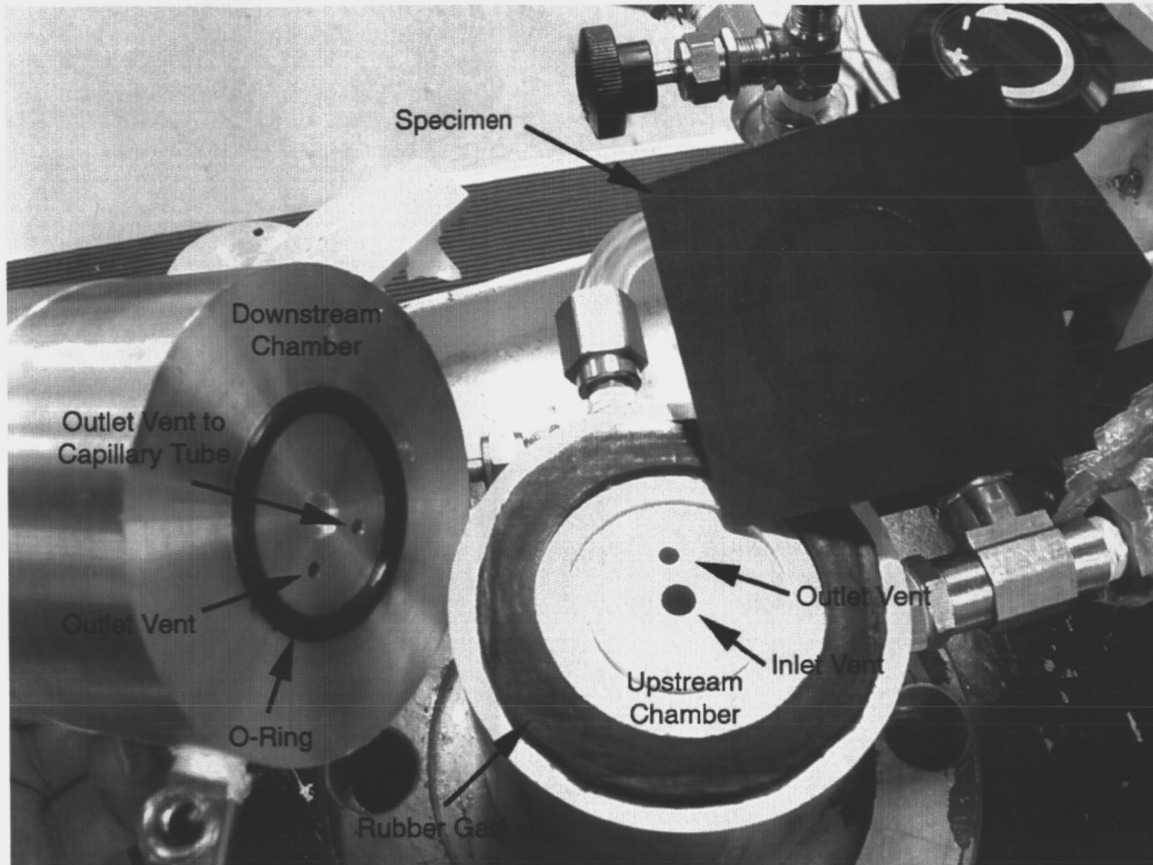


Figure 4-4. Specimen installation between upstream and downstream chambers.

The glass capillary tube is mounted on a rigid aluminum base horizontally to minimize the gravity effect on the capillary indicator and for easy reading of the scale marks on the capillary tube. Nettles [22] found that there was no significant difference in the volumetric flow rate when capillary tube is placed vertically or slanted. The inner diameter of the glass capillary tube is 1.05 mm and the length is 100 mm. A magnifying glass is used to read the scale marks at the top of the meniscus of the liquid indicator.

The liquid indicator in the glass capillary tube is used to measure the rate of rise of the liquid indicator. The rate is used to calculate the volume flow rate of the escaped gas across the specimen. Nettle [22] investigated the effects on the volume flow rates by using various types of liquid. The volume flow rates obtained using water, alcohol and alcohol with PhotoFlo[®] were not significantly different. In the present study, methyl alcohol is chosen as the liquid indicator since alcohol has low viscosity and weight. The methyl alcohol is colored with a blue dye to obtain precise readings on the scale marks.

The primary investigation is the hydrogen permeability of a liquid hydrogen composite storage system. Since hydrogen gas is highly flammable and explosive when it mixed with air, it needed to be handled carefully during the test. Hence, other permeate gases were considered as a substitute for the hydrogen gas. The molecular diameter of various gases is listed in Table 4-1 [23]. To choose a permeate gas, the molecular diameter determined from viscosity measurement is mainly considered since the permeability is

related with the volumetric flow rate directly. Since helium has the smallest molecular diameter, the helium predicts the permeation results higher than other gases [23]. Therefore, in the study, helium was chosen as the permeate gas instead of hydrogen.

Table 4-1. Molecular diameter of various gases from CRC Handbook of Chemistry and Physics, 54th Edition.

| Type of Gas | Molecular Diameter (cm) | | |
|-------------|-------------------------|------------------------------|------------------------|
| | From Viscosity | From van der Waal's Equation | From Heat Conductivity |
| Helium | 1.9×10^{-8} | 2.6×10^{-8} | 2.3×10^{-8} |
| Hydrogen | 2.4×10^{-8} | 2.3×10^{-8} | 2.3×10^{-8} |
| Nitrogen | 3.1×10^{-8} | 3.1×10^{-8} | 3.5×10^{-8} |

Specimen Description

The permeability tests were performed with various composite material systems. The details of specimens are described in Table 4-2. The specimens C1, C2 and C3 are various graphite/epoxy laminated composites. The specimen T1 is a textile composite. The specimen N1 is a laminated composite embedded with 36 μm aluminum oxide (Al_2O_3 -alumina) nano-particles. The aluminum oxide was dissolved in alcohol and the compound was applied on a surface on a laminated prepreg using a paint brush. The nano-particles are capable of relieving the thermal stresses due to contraction of fiber and matrix phases. Also, it can prevent the crack propagation in matrix phase by relieving the stress concentration at the crack-tip.

The graphite/epoxy prepregs were fabricated with designed stacking orientations. The graphite/epoxy prepregs were cured in an autoclave and machined by a diamond saw to 3×3 inch specimens at low speed to avoid fiber shattering. The surface is cleaned with acetone and prepared carefully to avoid contamination or damages on the surface of the specimen during machining and subsequent handling.

Table 4-2. Description of composite specimens.

| Specimen | Preprag Type | Stacking Sequence | Thickness (mm) |
|----------|--|----------------------|----------------|
| C1 | Graphite/Epoxy laminates | $[0/90/0/90/0/90]_S$ | 1.52 |
| C2 | Graphite/Epoxy laminates | $[0_2/90_2/0_2]_T$ | 0.787 |
| C3 | Graphite/Epoxy laminates | $[0/90/0_2/90/0]_T$ | 0.914 |
| C5 | Graphite/Epoxy laminates | $[0/90_2/0]_T$ | 0.533 |
| T1 | Plain weave textile(SP Systems SE-84) | 4 layers | 0.686 |
| N1 | Graphite/Epoxy laminates with nano-particles | $[0/90/NP/90/0]_T$ | 0.483 |

The specimens were subjected to cryogenic cycling at specified number of times, representing multiple refueling process of a space vehicle. A single cryogenic cycle consisted of cooling down from room temperature to cryogenic temperature and then warming up to room temperature. Initially, specimens were placed at room temperature ($T=300\text{K}$). And, then the specimens completely submerged in an insulated container

filled with liquid nitrogen. The specimens stayed in the container for approximately 2 minutes. When the specimen reached the boiling temperature of liquid nitrogen ($T = 77\text{K}$), the liquid nitrogen boiling disappears. The specimens were taken out of the container and placed at room temperature. The specimen was held at room temperature for approximately 5 minutes. The cryogenic cycling procedure is repeated for desired number of times.

Testing Procedure

Before starting the permeability test, a thin coat of silicon grease was applied on the gasket and an O-ring was placed to improve sealing of contact surfaces on a specimen. The excessive silicon grease was wiped out to avoid obstructions of permeated gas on the transmitting surface of the specimen. All outlet valves were opened initially to avoid sudden pressurization of test gas. The specimen was placed horizontally on the gasket of the upstream chamber. And then, the downstream chamber was placed on the top surface of a specimen. The specimen was mounted between the chambers. Both chambers were aligned and mated as close as possible. The specimen was mounted between the chambers and clamped firmly with a compressive force. Then, even distributed forces were applied to the sealing materials of the chambers.

The test gas was admitted to the upstream chamber by opening the gas release valve of the gas tank. While all outlet valves remained opened, the test gas was filled in the upstream chamber and ventilated through the outlet vent to atmosphere. Any residual air in the upstream chamber was purged for 1 minute. The outlet valve on the upstream chamber was closed and the test gas was allowed to permeate across the specimen for a sufficient time to purge any residual air at downstream chamber. At this time, only test gas filled the chambers. When the outlet valve of the upstream chamber was closed, the upstream pressure increased slowly. The upstream pressure can be adjusted by controlling the pressure regulator. Sufficient time was allowed for attaining steady state of moving rate of the liquid indicator before beginning to take readings. The distance of rise of the liquid indicator was measured while the ambient pressures were recorded.

Calculations

The volumetric methodology is used to calculate the permeability by measuring gas volume transmitted through a specimen. The rate of rise of the liquid indicator is measured using the capillary tube. The volume flow rate is calculated as follows.

$$V_r = \text{slope} \times a_c \quad (4.1)$$

where a_c is the cross-sectional area of a capillary tube. The slope is the rate of rise of the liquid indicator in the capillary tube. The gas transmitted rate (GTR) is calculated using the ideal gas law as follows.

$$GTR = \frac{P_o \cdot V_r}{ART} \quad (4.2)$$

where p_o is ambient pressure, A is transmitting area of a specimen, R is the universal gas constant ($8.3143 \times 10^3 \text{ L}\cdot\text{Pa}/\{\text{mol}\cdot\text{K}\}$) and T is ambient temperature. The permeance P is defined by the ratio between the gas transmission rate and pressure differential across the thickness of a specimen. Therefore, the permeance P is calculated as follows.

$$P = \frac{GTR}{p - p_o} \quad (4.3)$$

where p is the upstream pressure. The S.I. units of permeance are $[\text{mol}/(\text{m}^2 \cdot \text{s} \cdot \text{Pa})]$

According to the standard test method, the permeability \bar{P} is defined by the product of permeance P and the specimen thickness t and “the permeability is meaningful only for homogeneous materials [18].” In this study, although the laminated composites are considered as orthotropic materials, its permeability \bar{P} is calculated by following the corresponding definition for isotropic materials [22].

Calibration

The position of capillary indicator is very sensitively to even small variations of testing conditions such as ambient pressure and temperatures caused by closing doors or air-conditioning system in the laboratory. For example, during one test, the variation of the ambient pressure was approximately 0.3% for a 13 hour period (Figure 4-5). For the permeability calculation, the ambient pressure is assumed to be constant. However, the variation is large enough to cause error in measuring the rate of rise of the capillary indicator. The moving distance is needed to be calibrated to compensate for error due to the variation of ambient pressure.

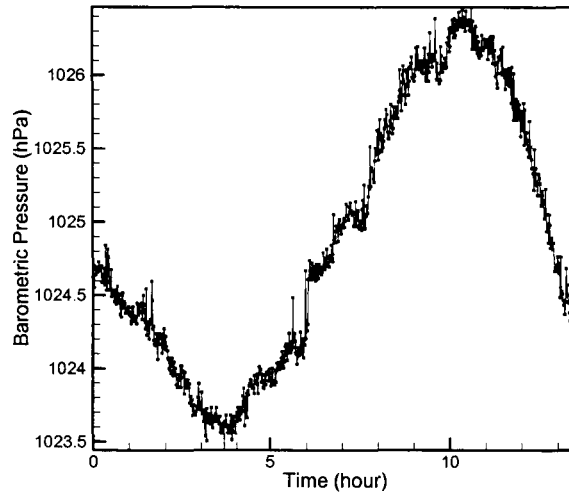


Figure 4-5. Variation of ambient pressure for 13 hours at test condition.

The error correction factor due to the variation of ambient pressure was calculated by performing the permeability test without applying the upstream pressure. An aluminum plate is used for the test to ensure that there is no gas permeation to the downstream chamber. Since there was not much variation in the ambient temperature, only ambient pressure causes changes in the position of the capillary indicator. After the outlet valve of the downstream chamber was closed, the displaced position of the capillary indicator and ambient pressure were measured simultaneously as shown in Figure 4-6.

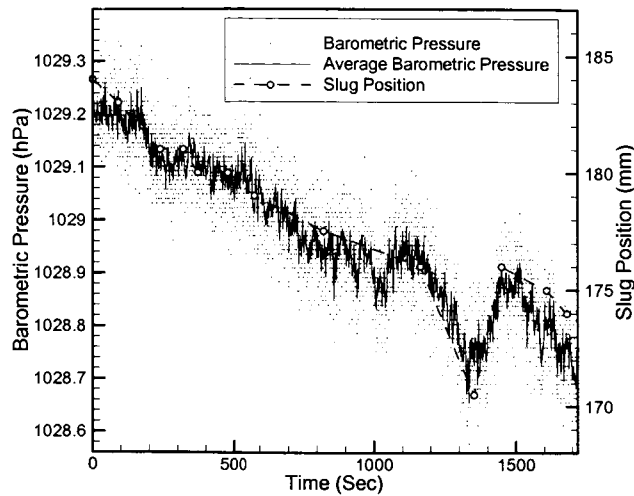


Figure 4-6. Variation of barometric pressure and indicator position as a function of time.

The correction factor k is calculated by $k = \Delta h / \Delta p$ where h is the moving distance of the capillary indicator and p is the ambient pressure. The average correction factor is found to be 0.21 mm/Pa. Therefore, the corrected moving distance of the capillary indicator is calculated as follows:

$$h_{corrected} = h_{actual} + k \cdot \Delta p$$

where Δp is differential of ambient pressure between the beginning and end of the test.

Permeability Test Results

The permeability tests were performed with various composite material systems at room temperature. The permeability was measured at six different levels of upstream pressure. The average permeance P and average permeability \bar{P} are tabulated in Table 4-3 for laminated composites, the results for textile composites are in Table 4-4 and the results for laminated composites with embedded with nano-particles in Table 4-5.

Table 4-3. Permeability of laminated composites for various number of cryogenic cycles.

| Specimen | Cryogenic cycles | Permeance, P (mol/sec/m ² /Pa) | Permeability, \bar{P} (mol/sec/m/Pa) | Logarithm of \bar{P} |
|----------|------------------|--|---|---------------------------|
| C1 | 0 | 5.60×10^{-18} | 8.54×10^{-21} | -20.1 |
| | 1 | 1.52×10^{-17} | 2.32×10^{-20} | -19.6 |
| | 5 | 2.39×10^{-17} | 3.65×10^{-20} | -19.4 |
| | 10 | 2.39×10^{-17} | 3.65×10^{-20} | -19.4 |
| | 20 | 2.11×10^{-17} | 3.22×10^{-20} | -19.5 |
| C2 | 0 | 7.02×10^{-18} | 1.07×10^{-20} | -20.0 |
| | 1 | 1.06×10^{-17} | 1.62×10^{-20} | -19.8 |
| | 5 | 1.47×10^{-15} | 2.23×10^{-18} | -17.7 |
| | 10 | 1.42×10^{-15} | 2.16×10^{-18} | -17.7 |

| | | | | |
|----|----|------------------------|------------------------|-------|
| | 20 | 1.49×10^{-15} | 2.27×10^{-18} | -17.6 |
| C3 | 0 | 6.22×10^{-18} | 9.48×10^{-21} | -20.0 |
| | 1 | 7.56×10^{-18} | 1.15×10^{-20} | -19.9 |
| | 5 | 7.60×10^{-18} | 1.16×10^{-20} | -19.9 |
| | 10 | 8.37×10^{-18} | 1.28×10^{-20} | -19.9 |
| C5 | 0 | 5.85×10^{-18} | 8.92×10^{-21} | -20.0 |
| | 1 | 9.52×10^{-16} | 1.45×10^{-18} | -17.8 |
| | 5 | 8.67×10^{-16} | 1.32×10^{-18} | -17.9 |
| | 20 | 8.81×10^{-16} | 1.34×10^{-18} | -17.9 |

Table 4-4. Permeability of textile composites for various number of cryogenic cycles.

| Specimen | Cryogenic cycles | Permeance, P (mol/sec/m ² /Pa) | Permeability, \bar{P} (mol/sec/m/Pa) | Logarithm of \bar{P} |
|----------|------------------|--|---|---------------------------|
| T1 | 0 | 4.79×10^{-18} | 7.30×10^{-21} | -20.1 |
| | 1 | 6.77×10^{-18} | 1.03×10^{-20} | -20.0 |
| | 5 | 8.41×10^{-18} | 1.28×10^{-20} | -19.9 |
| | 20 | 8.75×10^{-18} | 1.33×10^{-20} | -19.9 |

Table 4-5. Permeability of laminated composites embedded with nano-particles for various number of cryogenic cycles.

| Specimen | Cryogenic cycles | Permeance, P (mol/sec/m ² /Pa) | Permeability, \bar{P} (mol/sec/m/Pa) | Logarithm of \bar{P} |
|----------|------------------|--|---|---------------------------|
| N1 | 0 | 6.82×10^{-18} | 1.04×10^{-20} | -20.0 |
| | 1 | 2.72×10^{-15} | 4.15×10^{-18} | -17.4 |
| | 5 | 1.30×10^{-14} | 1.98×10^{-17} | -16.7 |
| | 20 | 9.83×10^{-15} | 1.50×10^{-17} | -16.8 |

The test results show the permeability increases as the number of cryogenic cycles increases (see Figure 4-7). The permeability increased rapidly and becomes constant with further increase of cryogenic cycles. For specimens C2 and C3, which have approximately same thickness, the permeability of the specimen C3 was lower since the specimen C3 has the plies dispersed and not grouped together compared to the specimen C2.

The textile specimen T1 maintained constant permeability with the increase of cryogenic cycles. The textile composites resulted lower permeability than the laminated composites.

The specimen N1 has same layer stacking orientations with the specimen C5 and nano-particles were dispersed between two 90-degree layers. Before cryogenic cycling, the permeabilities of the specimens N1 and C5 were approximately the same. However, as the number of cryogenic cycles increased, the permeability of the specimen N1 became

higher. The use of nano-particles did not improve the permeability of laminated composites.

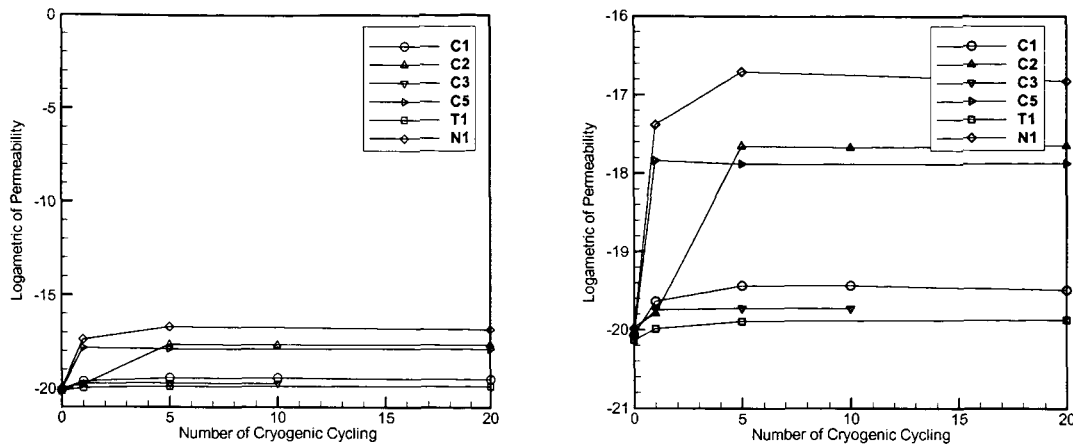


Figure 4-7. Logarithm of the permeability for composite specimens with increase of cryogenic cycles.

Optical Microscopic Analysis

The optical microscopic inspection was performed to evaluate the microcrack propagation and void content of various composite systems after cryogenic cycling. In the previous section, the experimental results showed that the permeability increases as the composite specimen underwent more cryogenic cycles. As the crack density increases, gas flow becomes easier through the specimen. Therefore, the microcrack propagation is correlated with cryogenic cycling.

The specimens were cut through the center using a diamond saw. A LECO grinder/polisher was used for the sample preparation process. The rough edge through the center was ground with 600-grit sand paper with water for 30 seconds. The fine grinding was performed with the 1000-grit and 1500-grit papers for 30 seconds. The surface of the edge was polished with the 58 μ m aluminum oxide powder (Al_2O_3 -alumina) dissolved in distilled water. The purpose of the lubricant is to both dissipate the heat from polishing and to act as a carrier for the abrasive materials. The ultrasonic cleaner was used to remove any abrasive particles and contaminants on the polished surface of a specimen. The optical analysis was conducted with a NIKON EPIPOT microscope.

The laminated composite specimen C2 and the textile composite specimen T1 were chosen for optical inspection. The specimen details are described in Table 4-2. The microscopic images for the specimens were compared before and after cryogenic cycling.

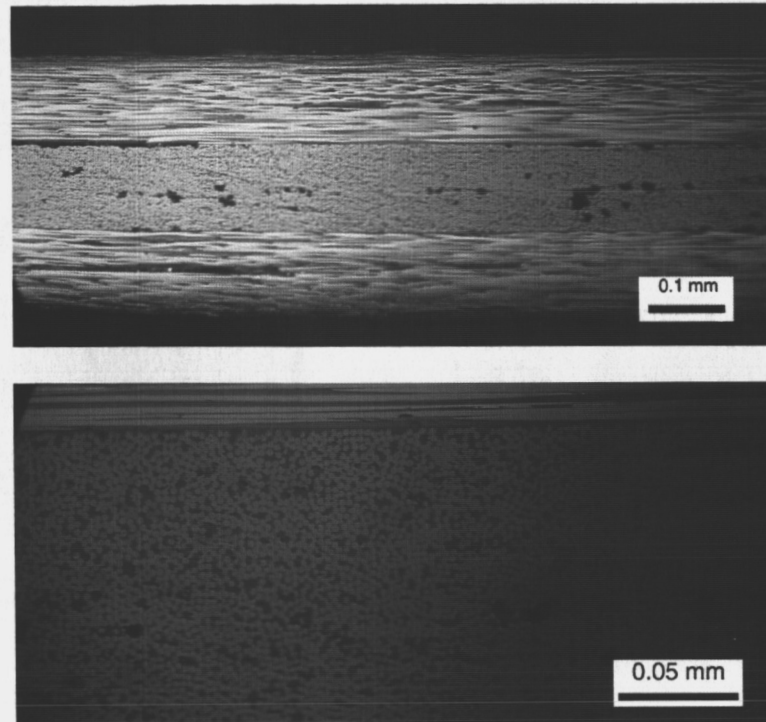


Figure 4-8. Cross sectional view of the graphite/epoxy composite specimen C2 before cryogenic cycling: (a) 10X magnification; (2) 40X magnification.

For the graphite/epoxy specimen C2 before cryogenic cycling, no microcrack propagation observed (see Figure 4-8). Some voids formed in the middle of the 90-degree layers and between the 0-degree layer and the 90-degree layers. The voids probably formed during composite fabrication in autoclave. When the graphite/epoxy prepreg was cured at high temperature, some air bubbles could have been trapped between layers. It is possible that external pressure applied on the vacuum bag was insufficient to remove the bubbles.

After cryogenic cycling on the specimen C2, microcracks were observed in the 90-degree layer as shown in Figure 4-9. The fiber breaks were not observed in the in 0-degree layer were not observed since the thermal stresses were not large enough. The delaminations propagated along the middle of the 90-degree layer where some voids were found. The transverse cracks branched with the delaminations. Since the gas can be transmitted through the transverse cracks across the specimen, the permeability increased after cryogenic cycling.

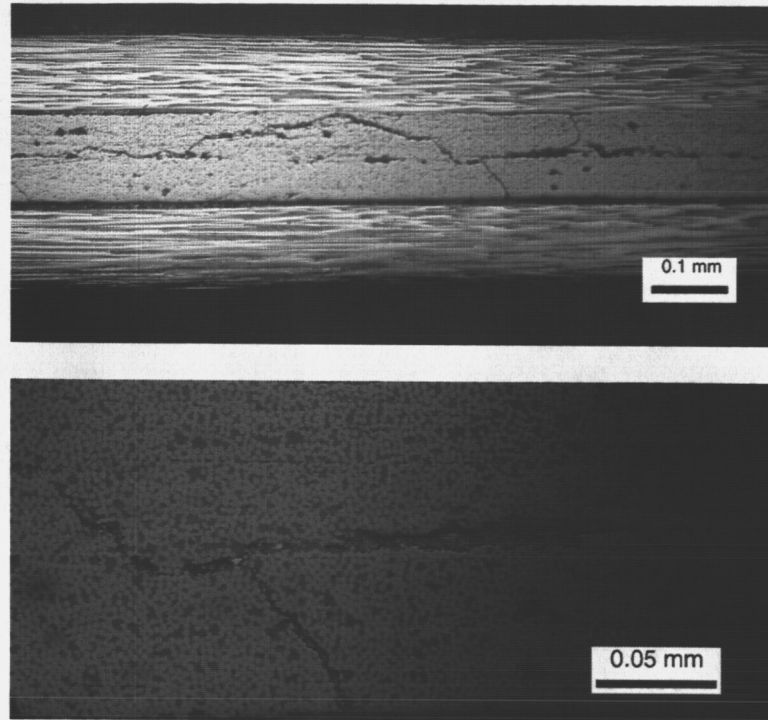


Figure 4-9. Microcrack propagation on the graphite/epoxy composite specimen C2 after cryogenic cycling: (a) 10X magnification; (2) 40X magnification.

For the textile composite specimen T1 before cryogenic cycling, no microcracks were observed as shown in Figure 4-10. Voids were observed at the location where two yarns are merging.

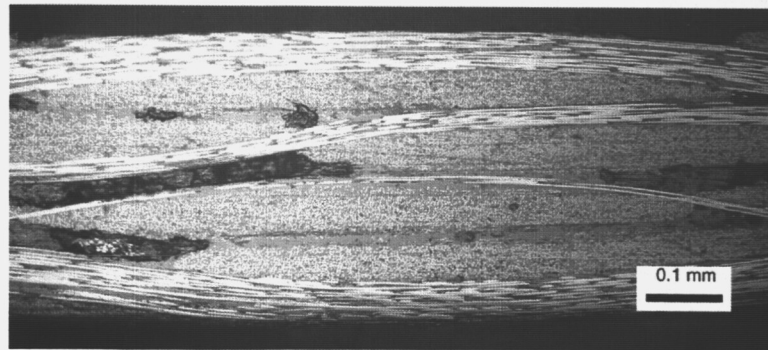


Figure 4-10. Cross sectional view of the textile specimen T1 before cryogenic cycling, 10X magnification.

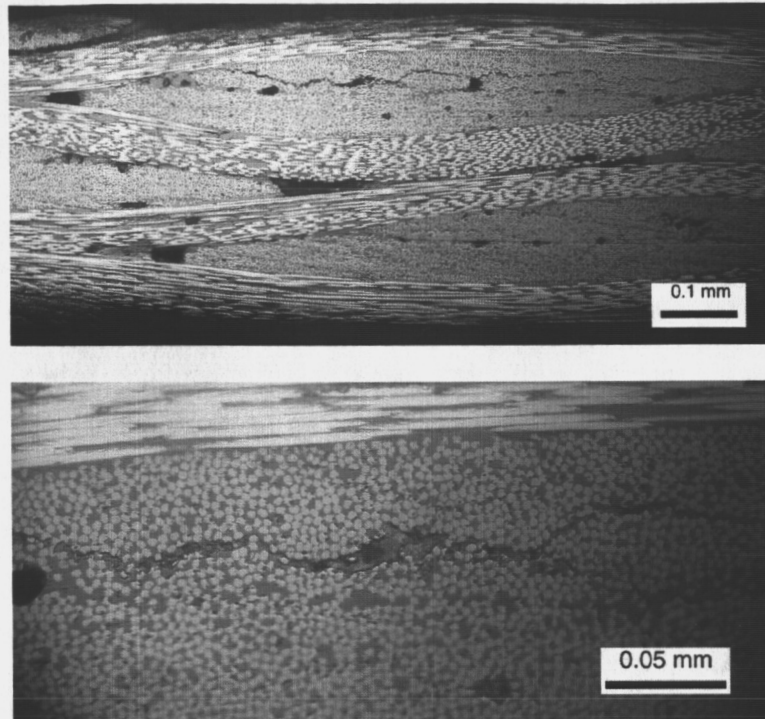


Figure 4-11. Microcrack propagation in the textile specimen T1 after cryogenic cycling: (a) 10X magnification; (b) 40X magnification.

After the textile specimen T1 underwent cryogenic cycles, microcrack were observed in 90-degree yarn as shown in Figure 4-11. The microcracks propagated in the in-plane direction of the specimen. Since transverse cracks were not propagated, the permeability of textile composites was almost the same before and after cryogenic cycling.

The transverse cracks and delaminations provide the leakage path through composite laminates and thus directly related to the permeability. For the laminated composite specimen, the microscopic results showed that transverse crack propagation and delaminations of composite laminates. For the textile composite specimen, the transverse cracks propagation was not observed, which resulted low permeability of textile composites even after cryogenic cycling.

CHAPTER 5

RESULTS AND DISCUSSION

The liquid hydrogen cryogenic composite tank proposed for future space vehicles will be exposed to extreme thermal and mechanical loads. During cryogenic cycling, the liquid hydrogen composite tank can fail due to the thermal stresses combined with structural loads. The present study is concerned with three of the several fundamental mechanics issues involved in the design of cryogenic composite tanks. First, the micro-stresses in the fiber and matrix phases of composite laminates were estimated at cryogenic temperature. Second, the fracture behavior of composite laminates at cryogenic temperature was predicted using the finite element method in conjunction with experimental analysis. Third, the permeability of various composite material systems for the liquid hydrogen composite storage system was investigated. The results from this study will be useful in the design of lightweight composite tanks for cryogenic storage systems.

Micromechanics Method to Predict Thermal Stresses for Laminated Composites at Cryogenic Temperature

A micromechanics model is developed from the repetitive patterns of the fiber distribution in the microstructures of composite laminates. The representative volume element was modeled using the square and hexagonal shapes depend on the fiber and matrix layout in microscopic images of composite laminates. The periodic boundary conditions were applied to the unit cell model to match the boundary displacements with adjacent unit cells. The epoxy resin is considered as homogeneous thermo-elastic material and the fiber properties are considered to be independent to temperature changes. The laminate properties were estimated using the micromechanics methods. The micromechanics methods made a good agreement with the semi-empirical solutions. The transverse properties estimated from the micromechanics model was used to verify the transverse isotropy of the composite laminates. The hexagonal unit cell satisfies the transverse isotropy better than the square unit cell. Therefore, the hexagonal unit cell is more realistic and better model for the micromechanics methods.

The micromechanics method yields detailed micro-stress distribution in the fiber, matrix and the interface between the fiber and matrix phases. These micro-stresses can be used to predict possible microcrack propagation of the composite at various temperatures with or without external loads. When a unidirectional laminate is subjected to free boundary conditions, the laminate stresses are zero from the stress-strain relation. However, the microstresses in fiber and matrix phases exist since the coefficient of thermal expansion of constituents are different. When the unidirectional laminate is subjected to cryogenic temperature, the thermal contraction between fiber and matrix phases causes the microstresses. The microstress results are compared with the material strength to predict the possible microcrack propagation. The method was used to analyze the micro-stresses in the liquid hydrogen composite tank. When the composite tank is subjected to cryogenic temperature without external loads, the micro-stresses did not exceed the material strength of the constituents. When the internal pressure of the composite tank reaches 10KPa at cryogenic temperature, the stresses in the matrix phase seem to exceed the tensile strength of the matrix material indicating micro-cracking is a possibility.

However matrix strength measured at cryogenic temperatures should be used for accurate prediction of formation of micro-cracks.

Fracture Toughness for a Transverse Crack in Laminated Composites at Cryogenic Temperatures

At cryogenic temperature, the transverse cracks propagate mostly at transverse plies of composite laminates. The transverse crack and delamination provide the leakage path of the liquid hydrogen permeation which causes the catastrophic failure of the composite tank. The stress singularity describes the fracture propagation of composite laminates. The singularities for glass/epoxy and graphite/epoxy composites with various stacking orientations are estimated using analytical and finite element methods. Singularities calculated by both methods are in good agreement. The results provide the confidence of capturing the singularity using the finite element model. When the transverse crack propagates in the unidirectional laminates, the singularity becomes 0.5 as a general homogeneous material. When the transverse crack propagates from the 0-degree to the 90-degree layer, the singularity becomes larger than 0.5 and vice versa.

The finite element analysis was performed to estimate fracture toughness of a transverse crack under the fracture load measured from the fracture experiment. The results of fracture toughness are compared at room and cryogenic conditions. Four-point bending experiments are performed at room and cryogenic temperatures to obtain fracture loads of graphite/epoxy specimens. The specimens had different mid-ply thicknesses, i.e., the crack lengths were different in different specimens. The results of fracture load and fracture toughness are listed in Table 3-6. At room temperature, fracture load increases 8% when the mid-ply thickness increases 67%. However, the variation of fracture toughness is less than 0.5%. Fracture toughness is only dependent to local properties near a crack tip, but not global properties of the laminate system. At cryogenic temperature the fracture load decreases 15% with increase of mid-ply thickness. The fracture load significantly decreases due to the material degradation at cryogenic temperature. The thermal stresses cause microcrack propagation in the vicinity of the crack. Although the fracture loads decrease by 15% from Specimen 1 to Specimen 3, fracture toughness increases by only 5%. For both cases at room and cryogenic temperature, fracture toughness was estimated approximately as $58 \text{ MPa}\cdot\text{m}^{0.29}$. The result indicates fracture toughness is a characteristic property not governed by temperature changes. The analysis is useful to predict the transverse crack propagation of composite laminates under cryogenic conditions.

Permeability Testing for Laminated Composites for a Liquid Hydrogen Storage System

The experimental analysis was performed to measure the gas permeability various composite material systems for the liquid hydrogen composite tank and the effect of cryogenic cycling of composite laminates on the permeability was investigated. The permeability test facility was constructed following the standard test method documented in ASTM D1434-82 (Re-approved 1997). The permeability test was conducted at room temperature. The sensitivity of permeability measurement can be improved by increasing the gas transmission area of a specimen. Since hydrogen is flammable and explosive

when it mixed with air, the helium gas is substitute for hydrogen. The calibration is performed to compensate the ambient pressure differences during the test. The correction factor is found as 0.21 mm/Pa. The actual moving distance of the liquid indicator is calibrated by the correction factor.

The permeability results for the various materials are shown in Figure 4-9. The permeability of laminated composite was found to degrade after undergoing cryogenic cycling process. The thin laminate specimens C2 and C5, the permeability increases significantly after cryogenic cycling. For thick laminated specimens C1 and C3, the increase of permeability is less. The textile composite specimen T1 has lower permeability than laminated specimens and the variation of permeability is very small with the increase of cryogenic cycles. The laminated composites were embedded with nano-particles which are capable of reducing thermal stresses in the matrix phase. However, as results, the nano-particles did not show the improvement on permeability. Further studies are needed to investigate the effects of nano-particles. The optical analysis was performed to investigate the microcrack propagation and void contents of test specimens. The transverse cracks and delaminations provide the leakage path through composite laminates and thus directly related to the permeability. The optical micrographic analysis was performed to investigate the microcrack propagation and void contents of test specimens. For the laminated composite specimen, the microscopic results showed that transverse crack propagation and delaminations of composite laminates. For the textile composite specimen, the transverse cracks propagation was not observed, which resulted in low permeability of textile composites even after cryogenic cycling.

APPENDIX

STRESS SINGULARITY USING STROH'S METHOD

Stress singularity at a ply crack tip acting normal to an interface of composite laminates can be obtained using Stroh's method. The displacements u_i ($i=1,2,3$) are in the x_1 - x_2 plane as shown in Figure A.1.

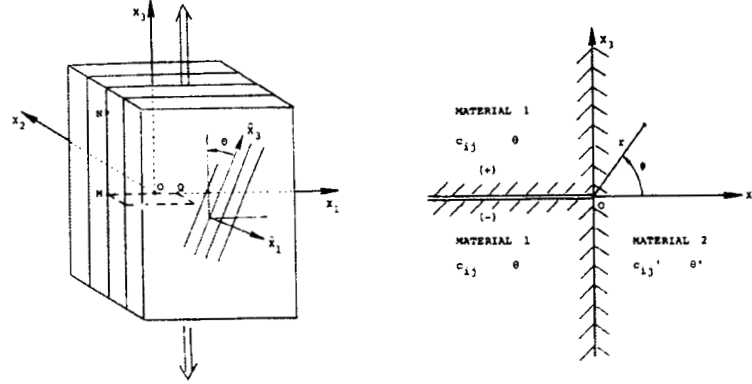


Figure A.1. Geometry of an angle-ply laminated composite and a crack normal to an interface between two anisotropic materials.

The strains and the stresses are described as a function of x_2 and x_3 . The displacement, stress-strain and equilibrium equations can be written as

$$\varepsilon_{ij} = (\partial u_i / \partial x_j + \partial u_j / \partial x_i) / 2 \quad (A1)$$

$$\sigma_{ij} = c_{ijkl} \varepsilon_{kl} \quad (A2)$$

$$\partial \sigma_{i2} / \partial x_2 + \partial \sigma_{i3} / \partial x_3 = 0 \quad (A3)$$

where $C_{ijkl} = C_{jikl} = C_{klij}$ are the elasticity constants. A general solution for Eqs. A1-A3 can be obtained by letting

$$u_i = v_i f(Z) \quad (A4)$$

$$Z = x_2 + p x_3 \quad (A5)$$

where p and v_i are constants to be determined and f is an arbitrary function of Z [14-15]. Substituting into Eqs. A1-A3, we obtain

$$\sigma_{ij} = \tau_{ij} df/dZ \quad (A6)$$

$$D_{ik} v_k = 0 \quad (A8)$$

where

$$\tau_{ij} = (c_{ijk2} + p c_{ijk3}) v_k \quad (A9)$$

$$D_{ik} = c_{i2k2} + p(c_{i2k3} + c_{i3k2}) + p^2 c_{i3k3} \quad (A10)$$

For a non-trivial solution of v_i , it follows from Eq. A8. that the determinant of D_{ik} must vanish. Therefore,

$$\|D_{ik}\| = 0 \quad (A11)$$

where

$$D_{11} = c_{1212} + p(c_{1213} + c_{1312}) + p^2 c_{1313} = c_{66} + p^2 c_{55}$$

$$\begin{aligned}
D_{12} &= c_{1222} + p(c_{1223} + c_{1322}) + p^2 c_{1323} = p(c_{46} + c_{25}) \\
D_{13} &= c_{1232} + p(c_{1233} + c_{1332}) + p^2 c_{1333} = c_{46} + p^2 c_{35} \\
D_{21} &= c_{2212} + p(c_{2213} + c_{2312}) + p^2 c_{2313} = p(c_{46} + c_{25}) \\
D_{22} &= c_{2222} + p(c_{2223} + c_{2322}) + p^2 c_{2323} = c_{22} + p^2 c_{44} \\
D_{23} &= c_{2232} + p(c_{2233} + c_{2332}) + p^2 c_{2333} = p(c_{23} + c_{44}) \\
D_{31} &= c_{3212} + p(c_{3213} + c_{3312}) + p^2 c_{3313} = c_{46} + p^2 c_{35} \\
D_{32} &= c_{3222} + p(c_{3223} + c_{3322}) + p^2 c_{3323} = p(c_{23} + c_{44}) \\
D_{33} &= c_{3232} + p(c_{3233} + c_{3332}) + p^2 c_{3333} = c_{44} + p^2 c_{33}
\end{aligned} \tag{A12}$$

Therefore, Eq. A12 is written as

$$\begin{bmatrix} c_{11} + p^2 c_{55} & p(c_{46} + c_{25}) & c_{46} + p^2 c_{35} \\ & c_{22} + p^2 c_{44} & p(c_{23} + c_{44}) \\ \text{Sym} & & c_{44} + p^2 c_{33} \end{bmatrix} \begin{Bmatrix} v_1 \\ v_2 \\ v_3 \end{Bmatrix} = 0 \tag{A13}$$

$$\begin{bmatrix} c_{55} & 0 & c_{35} \\ p_L^2 & 0 & c_{44} \\ c_{35} & 0 & c_{33} \end{bmatrix} + p_L \begin{bmatrix} 0 & c_{46} + c_{25} & 0 \\ c_{46} + c_{25} & 0 & c_{23} + c_{44} \\ 0 & c_{23} + c_{44} & 0 \end{bmatrix} + \begin{bmatrix} c_{11} & 0 & c_{46} \\ 0 & c_{22} & 0 \\ c_{46} & 0 & c_{44} \end{bmatrix} \begin{Bmatrix} v_1 \\ v_2 \\ v_3 \end{Bmatrix} = 0 \tag{A14}$$

The constant P_L exists in every term of the coefficient matrix in Eq. A14. Although it is possible solve for the root of the characteristic equation, numerical solutions to this type of problem yield more accurate eigenvalues. Hence Eq. A14 is further developed into an eigenvalue problem where P_L are complex eigenvalues with corresponding complex eigenvectors, v_{ij} where the L subscript associates the eigenvector with the appropriate eigenvalue ($L=1,2,3$). The equation is simplified as

$$[p^2[A'] + p[B'] + [C']][v] = 0 \tag{A15}$$

Multiply equation by the inverse of the coefficient matrix $[A']$.

$$[p^2[I] + p[B] + [C]][v] = 0 \tag{A16}$$

The eigenvalue equation is

$$[[A]_{6 \times 6} - \lambda[I]][Z] = 0 \tag{A17}$$

where the array $[A]$ can be constructed such that

$$[A] = \begin{bmatrix} -[B] & -[C] \\ [I] & [0] \end{bmatrix}_{6 \times 6} \tag{A18}$$

$$\lambda\{Z\} = [A]\{Z\} = [A] \begin{Bmatrix} \{x\} \\ \{y\} \end{Bmatrix} = \begin{bmatrix} -[B] & -[C] \\ [I] & 0 \end{bmatrix} \begin{Bmatrix} \{x\} \\ \{y\} \end{Bmatrix} = \begin{Bmatrix} -[B]\{x\} - [C]\{y\} \\ \{x\} \end{Bmatrix} \tag{A19}$$

where

$$\{Z\} = \begin{Bmatrix} \{x\} \\ \{y\} \end{Bmatrix}, \{x\} = \begin{Bmatrix} X_1 \\ X_2 \\ X_3 \end{Bmatrix} = \begin{Bmatrix} Z_1 \\ Z_2 \\ Z_3 \end{Bmatrix}, \{y\} = \begin{Bmatrix} Y_1 \\ Y_2 \\ Y_3 \end{Bmatrix} = \begin{Bmatrix} Z_4 \\ Z_5 \\ Z_6 \end{Bmatrix} \tag{A20}$$

$$\begin{cases} \lambda\{X\} \\ \lambda\{Y\} \end{cases} = \begin{cases} -[B]\{X\} - [C]\{Y\} \\ \{X\} \end{cases} \quad (\text{A21})$$

$$\lambda\{x\} = -[B]\{X\} - [C]\{Y\} \quad \text{and} \quad \{X\} = \lambda\{Y\}$$

These two equations can be combined into one equation by substituting for X , hence eliminating X , and rearranging terms.

$$[\lambda^2[I] + \lambda[B] + [C]]\{Y\} = 0 \quad (\text{A22})$$

Comparing Eq. A22 yield the necessary eigenvalues and eigenvectors

$$\lambda = P_L \quad \text{and} \quad \{Y\} = \begin{Bmatrix} Y_1 \\ Y_2 \\ Y_3 \end{Bmatrix} = \begin{Bmatrix} Z_4 \\ Z_5 \\ Z_6 \end{Bmatrix} = \{v\} \quad (\text{A23})$$

Comparing Eq. A23 and verifies that equation can be used to solve for P_L as eigenvalues instead of roots to the characteristic equation derived from the determinate of the coefficient matrix in equation. Both eigenvalues, P_L , and eigenvectors from equation will be used in the next section to calculate the singular exponent. The general solution of the displacement and stress is formulated using the Stroh's method Ting and Hoang [1].

$$u_i = r^{1-k} \sum \{a_L \operatorname{Re}(v_{i,L} \zeta_L^{1-k}) + \tilde{a}_L \operatorname{Im}(v_{i,L} \zeta_L^{1-k})\} / (1-k) \quad (\text{A24})$$

$$\sigma_{ij} = r^{1-k} \sum \{a_L \operatorname{Re}(\tau_{ij,L} \zeta_L^{-k}) + \tilde{a}_L \operatorname{Im}(\tau_{ij,L} \zeta_L^{-k})\} \quad (\text{A25})$$

where

$$\zeta = \cos \phi + p \sin \phi$$

where Re and Im stand for real and imaginary. Since the material 1 is divided into two parts by a crack, the displacements and the stresses in the Material 1 has superscript of (+) or (-). A superscript (+) to denote properties of the Material 1 in the positive region of the x_1 and (-) to denote properties of Material 1 in the negative region of the x_1 axis. The stress free boundary conditions at the crack surface are

$$\begin{aligned} \sigma_{1j}^+ &= 0 \quad \text{at} \quad \phi = \pi \\ \sigma_{1j}^- &= 0 \quad \text{at} \quad \phi = -\pi \end{aligned} \quad (\text{A26})$$

The continuity conditions at the interface are

$$u_i^+ - u_i^- = 0 \quad \text{at} \quad \phi = \pi/2 \quad (\text{A27})$$

$$\sigma_{2i}^+ - \sigma_{2i}^- = 0 \quad \text{at} \quad \phi = \pi/2$$

$$u_i^+ - u_i^- = 0 \quad \text{at} \quad \phi = -\pi/2 \quad (\text{A28})$$

$$\sigma_{2j}^+ - \sigma_{2j}^- = 0 \quad \text{at} \quad \phi = -\pi/2$$

Using the displacement and stress equations, the boundary and the continuity equation results in 18 equations for the eighteen coefficients of A_L^+ , B_L^+ , A_L' , B_L' , A_L^- and B_L^- . The equations can be written in matrix form

$$K(\kappa)q = 0 \quad (\text{A29})$$

where K is an 18×18 square matrix and the elements of q are A_L^+ , B_L^+ , A_L' , B_L' , A_L^- and B_L^- . For a nontrivial solution of q , determinant of the matrix K must be zero when singularity λ satisfies the matrix K . The determinant was calculated numerically.

LIST OF REFERENCES

1. Final report of the X-33 Liquid Hydrogen Tank Test Investigation Team, Marshall Space Flight Center, Huntsville, AL, May 2000.
2. Marrey, R.V. and Sankar, B.V., "Micromechanical Models for Textile Structural Composites," *NASA Contractor Report*, 198229, October 1995.
3. Chen, C.H. and Cheng, S., "Mechanical Properties of Fibre Reinforced Composites," *Journal of Composite Material*, **1**, 30-40, 1967.
4. Teply, J. L and Dvorak, G.J., "Bounds on Overall Instantaneous Properties of Elastic-Plastic Composites," *Journal Mechanics and Physics Solids*, **36**, 29-58, 1988.
5. Paley, M. and Aboudi, J., "Micromechanical Analysis of Composites by the Generalized Cells Model," *Mechanics of Materials*, **14**, 127-139, 1992
6. Nedele, M. R. and Wisnom, M.R., "Finite Element Micromechanical Modeling of a Unidirectional Composite Subject to Axial Shear Loading," *Composites Science and Technology*, **25**, 263-272, 1994.
7. Marrey, R.V. and Sankar, B.V., "Micromechanical Models for Textile Structural Composites," *NASA Contractor Report*, 198229, 1995.
8. Sankar, B.V. and Marrey, R.V., "Analytical Method for Micromechanics of Textile Composites," *Composites Science and Technology*, **57**(6), 703-713, 1997.
9. Marrey, R.V. and Sankar, B.V., "A Micromechanical Model for Textile Composite Plates," *Journal of Composite Materials*, **31**(12), 1187-1213, 1997.
10. Li, S., "On the unit cell of micromechanical analysis of fibre-reinforced composites," *Proceeding of Royal Society London A*, **455**, 815-838, 1999.
11. Zak, A. K., and Williams, M. L., "Crack Point Singularities at a Bi-material Interface," *ASME Journal of Applied Mechanics*, **30**, 142-143, 1963.
12. Gupta, V., Argon, A.S. and Suo, Z., "Crack Deflection at an Interface between Two Orthotropic Media," *Journal of Applied Mechanics*, **59**, 79-87, June 1992.
13. Williams, M. L., "On the Stress Distribution at the Base of a Stationary Crack," *Journal of Applied Mechanics*, **24**, 109-114, 1957.
14. Ting, T.C.T and Chou, S.C., "Stress Singularities in Laminated Composites," *Fracture of Composite Materials*, eds. Proceedings of the 2nd USA-USSR Symposium, Lehigh Univ., Bethlehem, PA, March 9-12, 1981, 265-277, 1982.
15. Ting, T.C.T. and Hwang, P.H., "Singularities at the Tip of a Crack Normal to the Interface of an Anisotropic Layered Composite," *International Journal of Solids and Structures*, **20**(5), 439-454, 1984.
16. Hutchinson, J.W. and Suo, Z., "Mixed Mode Cracking in Layered Materials," *Advances in Applied Mechanics*, **29**, 63-191, 1991.
17. Stockes, E., "Hydrogen Permeability of Polymer Based Composite Tank Material Under Tetra-Axial Strain," Proceedings of the fifth conference on aerospace materials, processes and environment technology (AMPET), Huntsville, Alabama, September 16-18, 2002, http://www2.southernresearch.org/pdf/tetraaxial_strain.pdf, last accessed, May 20, 2005.
18. ASTM D1434-82 (Reapproved 1992), "Standard Test Method for Determining Gas permeability Characteristics of Plastic Film and Sheeting," ASTM, 203-213, 1992.

19. Kumazawa, H., Aoki, T. and Susuki, I., "Analysis and Experiment of Gas Leakage Through Composite Laminates for Propellant Tanks." AIAA Journal, **41**(10), 2037-2044, October 2003.
20. Grimsley, B., Cano, R., Johnston, N., Loos, A. and McMahon, W., "Hybrid Composites for LH2 Fuel Tank structure," Proceedings of the 33rd International SAMPE Technical Conference, NASA Langley Research Center, November 4-8, 2001.
21. Herring, H., "Characterization of Thin Film Polymers through Dynamic Mechanical Analysis and Permeation," NASA/CR-2003-212422, 2003.
22. Nettles, A.T., "Permeability Testing of Impacted Composite Laminates for Use on Reusable Launch Vehicles," NASA/TM-2001-210799, 2001.
23. Nettles, A.T., "Permeability Testing of Composite Materials and Adhesive Bonds for the DC-XA Composite Feedline Program," NASA Technical Memorandum 108483, March 1995.
24. Glass, E., Venkat, V. and Sankaran, S., "Honeycomb Core Permeability Under Mechanical Loads," NASA/CR-97-206263, 1997.
25. Horiuchi, T. and Ooi, T., "Cryogenic Properties of Composite Materials," *Cryogenics*, **35**: 677-679, 1995.
26. Agarwal, B. and Broutman, L., *Analysis and Performance of Fiber Composites*, 2nd Edn, John Wiley & Sons, Inc, New York, 1990.
27. Elseifi, M., "A New Scheme for the Optimum Design of Stiffened Composite Panels with Geometric Imperfections," Ph. D. dissertation, Virginia Polytechnic Institute and State University, Blacksburg, Virginia, 1998.
28. Hashin, Z., "Analysis of Composite Materials-A Survey," *Journal of Applied Mechanics*, **50**, 481-505, September, 1983.
29. Anderson, T.L., *Fracture Mechanics, Fundamentals and Applications*, 2nd Edn, CRC Press LLC, Boca Raton, Florida, 1994.